2022

Resonant Trojan EMRIs with LISA

Vanessa Myhaver
University of Vermont

Resonant Trojan EMRIs with LISA

A Thesis Presented

by

Vanessa Myhaver

to

The Faculty of the Graduate College

of

The University of Vermont

In Partial Fulfillment of the Requirements
For the Degree of Master of Science
Specializing in Complex Systems and Data Science

May, 2022

Defense Date: March 21st, 2022
Thesis Examination Committee:

Christopher Danforth, Ph.D., Advisor
William Louisos, Ph.D., Chairperson
Jeremy Schnittman, Ph.D.
Peter Sheridan Dodds, Ph.D.
Cynthia J. Forehand, Ph.D., Dean of the Graduate College

Abstract

Extreme–mass–ratio inspirals (EMRI) are prospective sources for the detection of observational signals with the Laser Interferometer Space Antenna (LISA) mission, built to accurately detect and measure gravitational waves – ripples in the curvature, and fabric of space–time. EMRIs are typically comprised of a supermassive black hole (SMBH) one million times more massive than our Sun, and a stellar–origin black hole several orders of magnitude smaller. As the smaller black hole spirals into the supermassive black hole, thousands of cycles of the gravitational waveform serve as a precision probe for the extreme space-time curvature of the system. The goal of this research is to model the dynamics of and calculate the gravitational waveforms from "Trojan analog" EMRIs: multiple EMRIs in a single system, locked in 1:1 resonant orbits, analogous to Jupiter's Trojan asteroids.

In this thesis we present and confirm the accuracy of the methods used to calculate the equations of motion of such a system using Newtonian, 1st post-Newtonian (PN), and 2.5 PN terms of motion with Hamiltonian Mechanics. Using the resulting motion of the three–body system, we present methods used to calculate the gravitational waves produced by the system's inspiral using the quadrupole formula. We then conduct a comparison test of the Resonant Trojan system to a Single, classical EMRI system which concludes that these Trojan EMRIs hold a mix of unique observational potentials, distinct from those of Single EMRI systems, that may be detectable with the LISA mission, while simultaneously providing detailed orbital dynamics around a supermassive black hole.

Acknowledgements

I would like to begin by thanking my two advisors/mentors Dr. Chris Danforth and Dr. Jeremy Schnittman for their inspiration, encouragement, support, and knowledge throughout the past two years of this project. I owe my sincerest gratitude to the two of them for making this degree and research possible. I am very thankful for my committee chair, Dr. William Louisos as he has always been an incredible source of academic discussion and support. I would also like to thank Dr. Peter Sheridan Dodds and the entire Computational Story Lab for assisting my development of this project with their insightful feedback over the past two years. Next I would like to thank all of my professors at UVM who have shared their vast academic backgrounds, guiding my education to acquire the knowledge necessary to conduct this research. To every professor that has provided their advisement, academic support, and care for my well-being, you have all made the difference of a lifetime in my education and your constant encouragement has pushed the boundaries on what I am capable of. To my friends, family, and partner, I thank you from the bottom of my heart for being the source of light throughout some of my most trying times. You have all fostered an environment of love and joy that I will forever be thankful for. Lastly, I would like to thank the Vermont Space Grant Colloquium, MassMutual Center of Excellence, NASA's LISA Project Study Team, SURA, and CRESST II for providing financial support for my education, internships, and current position at NASA Goddard where I conduct this research. This material is based upon work supported by NASA under award number 80GSFC21M0002. Any opinions, findings, and conclusions or recommendations expressed in this material are those of the author and do not necessarily reflect the views of the National Aeronautics and Space Administration.

Table of Contents

List of Figures

Chapter 1

Introduction

Gravitational waves are ripples in the fabric of space–time that remain undisturbed after creation and serve as a precision probe for the space–time curvature of any system [4], [5]. NSF's Laser Interferometer Gravitational–Wave Observatory (LIGO) is the first terrestrial interferometer to detect gravitational waves with a signal frequency band of 10 Hz − 10 kHz [6]. The Laser Interferometer Space Antenna (LISA) will be the first space–based gravitational wave detector, comprised of an equilateral triangular spacecraft configuration [7], [8]. The LISA mission is led by ESA with major contributions from NASA. The goal of this mission is to detect and accurately measure the gravitational waves of a lower frequency band ranging from 0.1 mHz−0.1 Hz, which is undetectable from terrestrial interferometers [4], [5], [7], [8].

Due to LISA's low–frequency sensitivity, this mission will unveil regions of space that are absent from light, inaccessible from electromagnetic observations. The LISA mission will be capable of detecting signals from coalescing supermassive black hole (SMBH) mergers, extreme and intermediate mass ratio inspirals (E/IMRI), galactic binaries, and stochastic gravitational-wave background [7], [9]. The observed gravitational wave signals from the LISA mission will expand our understanding of fundamental physics by testing General Relativity in the most extreme regimes through gravitational waveform phase and amplitude. Gravitational wave detection will also advance our understanding of astrophysics by mapping the environments around supermassive black holes. As supermassive black holes are expected to lie at the center of galaxies and create matter–rich systems, gravitational wave signals will allow us to identify the dynamics of objects that populate SMBH systems [4], [9].

In this thesis we will focus on LISA's detection of Extreme Mass–Ratio Inspirals (EMRIs). EMRIs are typically comprised of a supermassive black hole (SMBH)

with mass $[10^5 - 10^7]M_\odot$, and a stellar–origin black hole with mass $[1 - 100]M_\odot$. As the stellar–mass black hole spirals into the supermassive black hole, thousands of gravitational waveforms serve as a precision probe for the extreme space–time curvature of the system [5]. An EMRI system can form due to a stellar–mass BH being trapped by a SMBH or a collapse within the SMBH accretion disk, both of which will lead to an ultimate inspiral into the SMBH [8]. EMRI gravitational wave frequency falls within the LISA band and is expected to be one of the main detection targets for this mission. EMRIs are expected to provide us with detailed space–time dynamics around supermassive black holes as the stellar–mass black hole acts as a test–body for the SMBH, testing the Theory of General Relativity. EMRI detection will provide insight into parameters of individual systems, mass distributions, and stellar environments throughout the Universe as they act as probes for the dynamics of galactic nuclei [5]. Due to their extreme mass ratio, EMRIs follow a slow, gradual inspiral such that $\sim 10^4 - 10^5$ inspiral cycles fall within the LISA frequency band which will allow us to observe and measure EMRI parameters extensively [10], [11]. While the astrophysical uncertainties of EMRIs are complex, it has been estimated that the detection of EMRI systems from LISA ranges from at least a few detections per year to a few thousand per year with about three orders of magnitude of uncertainty and a signal–to–noise ratio of several hundred [10], [11], [12].

Due to their extreme gravitational pull, SMBHs are expected to be surrounded by a dense–matter accretion disk. Through random disruption or formation, it is possible for EMRI systems to capture a third stellar–mass black hole to create a three–body system [9]. These three–body black hole systems can create resonances, such that, the two stellar–mass black holes have characteristic frequencies that match

an integer–number ratio [13]. Due to this resonance, the two stellar–mass black holes fall into a stable periodic orbit, locked into orientation, with phase libration around a fixed point [14]. The resonant stellar–mass black holes will oscillate around this stable fixed point while continuing to inspiral towards the supermassive black hole. Various studies have looked at EMRI systems capturing a small third body with hierarchical resonance, but in this thesis, we examine a multiple EMRI system with 1:1 orbital resonance between the two stellar–mass black holes inspiraling towards the supermassive black hole.

For a three–body system with two bodies locked into 1:1 orbital resonance around a third, larger body, it has been shown that the only stable configuration of the three bodies consists of three bodies forming an equilateral triangle [15]. Other three–body configurations will lead to the ejection of the third body or a merger of the two stellar–mass black holes within the accretion disk of the central, supermassive black hole. This 1:1 resonant configuration is the only stable configuration such that all three bodies will merge simultaneously [16], [17]. For the purpose of this thesis, we will focus on the gravitational waveforms from "Trojan analog" EMRIs: multiple EMRIs in a single system, locked into a 1:1 resonant orbit, analogous to Jupiter's Trojan asteroids.

A French-Italian mathematician Joseph Lagrange wrote the "Essai sur le problème des trois corps" (Essay on the Three–Body Problem) [18] in which he researched a solution to the Three–Body Problem, a classical dynamics problem which incorporates the initial conditions of positioning and velocities of three massed bodies in a system. Using Newton's Laws of Motion and Universal Gravitation, the Three–Body Problem attempts to solve and understand the motion of all three bodies within the

system. Although the general solution to the Three–Body Problem is chaotic, within Lagrange's research he came across the discovery of the planar and circular Restricted Three–Body Problem, a system containing three bodies in which the third body has a negligible amount of mass and does not affect the motion and orbit pattern of the other two bodies in the system. Through Lagrange's research, he discovered his Lagrange points, which are five points within a three–body system in space that represent the location of the third, negligible–mass body in the Restricted Three–Body Problem. These five Lagrange points consist of three unstable points (L1, L2, and L3) and two stable points (L4 and L5), each forming a Restricted Three–Body system with the other two bodies in the system. For this three–body system to create a stable resonance, the first two masses must satisfy a mass ratio of $M_1/M_2 > 24.960$ [18].

These five points have been shown to exist in the natural world in Planet–Sun systems such as the Jupiter–Sun system with Trojan asteroids in the location of the L4 and L5 Lagrange points [15]. The stable, three–body equilateral triangle configuration discussed above is analogous to the Jupiter–Trojan system such that the supermassive black hole resides in the location of the Sun, the first stellar–mass black hole resides in the location of Jupiter, and the third massed object, the second stellar–mass black hole lies in the location of the L4 or L5 Lagrange point. As the L4 and L5 Lagrange points are symmetrical, for the purpose of this thesis we choose our third body to reside in the location of the L4 Lagrange point. This configuration of the three bodies in the Resonant Trojan EMRI system can be viewed in Figure 1.1.

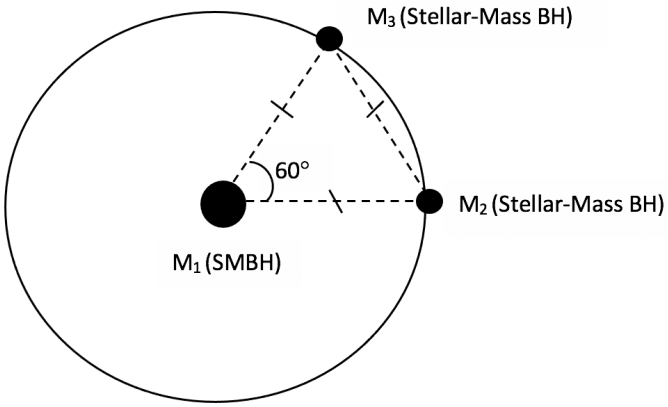

Figure 1.1: The stable, three black hole equilateral triangle configuration, analogous to the Jupiter–Trojan system. The supermassive black hole (M_1) resides in the location of the Sun, the first stellar–mass black hole (M_2) resides in the location of Jupiter, and the third object, the second stellar–mass black hole (M_3) lies in the location of the L4 Lagrange point.

While Lagrange found this stable restricted three–body system to have a negligible third mass, it has been shown that the system will remain stable when the two stellar–mass black holes in the system have comparable masses with the condition that the two stellar–mass black holes are small compared to the central, supermassive black hole [15]. In this thesis, we will look at an analogous multiple EMRI system such that by definition of an EMRI, the mass ratio between the SMBH and stellar–mass black holes satisfy this mass condition.

The objective of examining the Resonant Trojan EMRI system is to determine the potential orbital dynamics of the three bodies and simulate the gravitational wave signal expected from LISA given various initial parameters. In this thesis, we compare the dynamics and gravitational wave results of the Resonant Trojan EMRI with a Single EMRI system to identify whether there exists a unique difference in the expected gravitational signal detection from LISA. This provides an understanding

of EMRI system dynamics and their evolution, ultimately learning about the gravitational waves produced by such a system to gain knowledge about the environment and curvature of space–time around multiple EMRI systems.

To accurately calculate the equations of motion of such a system we use Newtonian, 1st post–Newtonian (PN), and 2.5 PN terms of motion with Hamiltonian Mechanics. The Hamiltonian approach is particularly suited for the classical mechanics of dynamical systems with resonant behavior, such as the system we are considering [14]. The Newtonian term takes into consideration terms of gravitational pull of each body while the post–Newtonian terms take into account terms of general relativity, the theory of gravitation developed by Albert Einstein to calculate the gravitational effect bodies have on each other based on their curvature of space–time. The 2.5 PN is a dissipative, gravitational radiation reaction term that considers the loss of energy and angular momentum within a system, ultimately leading to an inspiral of the given bodies [4], [19]. These equations are simulated using the Adaptive Runge–Kutta–Fehlberg Order 4–5 numerical integration method. Using the resulting position dynamics, we calculate the gravitational waveform produced by the three–body system using the quadrupole formula, as the LISA mission will detect both polarizations of gravitational wave signals [4]. We will show that the resulting gravitational waveform displays sensitive dependence upon initial condition [10], [20] due to the mass, position, and velocity of each body.

In this thesis, we first discuss related research studying the dynamics and gravitational waves of Resonant Trojan EMRIs along with previous papers that have used similar methods of calculation. Next, we present methods used to accurately calculate the equations of motion and gravitational waves produced by the system's

inspiral. We then conduct a comparison test of the Resonant Trojan system to a Single, classical EMRI system. First, we present the orbital dynamics of the Resonant Trojan systems, looking at short term differences in the gravitational wave results compared to those of a Single EMRI system. We then present the long–term inspiral results of Single and Resonant Trojan EMRI systems for various stellar–mass black hole mass–ratios.

Lastly, we conclude our findings from this comparison test, present the future work of this project, and emphasize the scientific importance of this work to both the LISA mission and to our understanding of EMRIs, three–body interactions, and general relativity. Modeling these orbital dynamics and gravitational wave signals provides us with information about the curvature of space–time around these three–body systems and the unique dynamics produced by the Resonant Trojan EMRI system compared to that of a Single EMRI system.

Chapter 2

Related Work

Post–Newtonian approximation is a method of solving Einstein's field equations for systems with slow motion and weak gravitational fields, but has been proven to be a highly effective method in strong-field, fast-motion systems such as a black hole system with gravitational radiation [21]. Since we are conducting a source comparison test of the waveforms produced by single and multiple EMRI systems using the post–Newtonian equations of motion within this thesis, we must validate our numerical integration of these equations for a two– and three–body system.

Bonetti, et al. [2] has produced an analysis of the numerical implementation of the 1PN, 2PN, and 2.5PN terms applied to three–body hierarchical black hole systems. We use a negligible third mass to simulate the motion of a two–body system to compare their results to the first–order coupled orbit–averaged equations for the time derivative of eccentricity and semi-major axis created by Peters and Mathews to numerically integrate the orbital evolution of a two–body system [1]. The evolution of the eccentricity and semi–major axis are related to the loss of energy and angular momentum due to the 2.5PN term [22]. Therefore, within their comparison to the Peters and Mathews orbit–averaged equations, Bonetti et al. includes only the 2.5PN term in the equations of motion for this analysis. They also examine the separation, circularity, and inclination between the inner binary of various eccentric three–body hierarchical systems. We replicate their methods and analysis to confirm our numerical implementation of the post–Newtonian terms using a Hamiltonian approach.

While many papers discuss two–body and three–body hierarchical systems, within this section we discuss previous work done on the understanding of Resonant Trojan three–body systems. Each of the following papers use the post–Newtonian approximation to simulate the motion of three–body systems, and the papers that discuss

gravitational waves use the quadrupole or octupole formulas to determine the resulting waveforms of these systems.

It has previously been found that the inclusion of the 1PN term in the equilateral triangular configuration leads to reduced stability compared to the Newtonian triangular configuration of the Restricted Three–Body Problem [23]. Yamada and Asada have found that the PN corrections for general relativity cause the triangular configuration to break its perfect equilateral positioning, while still remaining stable [24]. While various mass ratios and hierarchical three–body systems demonstrate chaotic evolution, even with consideration of the 2.5PN gravitational radiation reaction term, the Resonant Trojan system appears to remain stable long–term throughout the inspiral, maintaining its orbital plane, center of mass, and equilibrium while the system sees a loss of energy and angular momentum with increasing orbital frequency.

Numerous papers have discussed the sensitivity of the system's mass–ratio and initial separations on the stability of the equilateral triangular configuration when using PN approximation due to the relativistic effects of the system [16], [17], [24], [22], [25]. In this thesis, we consider various mass–ratios, initial separations, and initial velocities of the three bodies in Lagrange's equilibrium configuration to demonstrate the stable orbital dynamics as indicated by the system's sensitive dependence upon initial condition.

A previous paper by Seto and Muto [16] looks at a binary black hole system that traps a third body with negligible mass, located at either the L4 or L5 Lagrange point, considering the 1PN and 2.5PN terms of motion approximation. In their paper they find that due to gravitational radiation, the system will become less stable overtime. Based on the defined mass–ratio and separation of each body, they find that the

third negligible–mass body can be resonantly "held" by the system up to their final separation based on numerical precision. They state that due to the inspiral's reduced stability, it is possible that at close separations, the third negligible–mass body may be ejected from the system before merger. In either case, they state that the gravitational emission of the third body may allow us to probe various astrophysical effects based on the gravitational signal produced by the merger of such a system.

A similar paper by Schnittman [17] uses only the 2.5PN correction to look at a binary black hole system that traps a third body with negligible mass, located at either the L4 or L5 Lagrange point. He shows that with the inclusion of only the 2.5PN gravitational radiation term, the L4 point will move towards the secondary BH (in the analogous location of Jupiter), losing stability, and the L5 point will move away from the secondary BH, gaining stability. In this study, Schnittman constructs the gravitational waveforms of this Trojan analog system and finds that this circular–orbit system, with no libration of the secondary and negligible–mass third body, will be indistinguishable from a circular–orbit binary system, producing a pure sinusoidal gravitational waveform. He does state however that with libration of the second and third body, it is possible that the Trojan analog system will produce distinct signals detectable by the LISA mission.

In the two papers by Seto and Muto [16] and Schnittman [17], they state that a further analysis of the gravitational wave signals produced by the Resonant Trojan system will provide a deeper understanding of the system dynamics as well as the potential detection for the LISA mission. In this thesis, we confirm both the indistinguishable and distinct features of the Trojan analog system for the detection of EMRI systems with the LISA mission.

Two papers from Torigoe et al. [3] and Asada [26] conduct a gravitational wave comparison test of a binary source to the Resonant Trojan source with a non–negligible third body in the location of the Lagrange point. Using the gravitational–wave inverse problem to produce the evolution chirp mass of each system, they determine whether there exists a detectable difference in the gravitational waves produced by each system using Newtonian equations of motion and considering only perfectly circular orbits. Both papers conclude that the quadrupole formula used to calculate the gravitational waveforms does not present a distinguishable difference between the two systems, while the inclusion of the octupole formula demonstrates a recognizable difference between the two sources. These papers present the importance of including higher multipole terms to distinguish a difference in gravitational wave sources, as lower multipole terms will cause an indistinguishable gravitational signal between the two test sources.

In this thesis, we confirm their indistinguishable results from the quadrupole formula using PN approximations and simulate the resulting gravitational waves of each system instead of their analysis using the gravitational inverse problem. In the future of this research we will use the octupole formula to demonstrate the difference in gravitational waveforms as well as compute the expected chirp mass evolution of each system to confirm the results of this prior research and provide a more detailed orbital dynamic analysis. While these previous papers only consider perfectly circular orbits, in the future of this research we will also explore the possibility of detecting libration motions in the gravitational waveforms, unique to the three–body system.

Chapter 3

Methods

3.1 Equations of Motion

In the scope of this paper, we present numerous EMRI systems with varying initial conditions. For our three–body EMRI system we define the central, supermassive black hole to have mass m_1, the analogous Jupiter, stellar–mass black hole to have mass m_2, and the Lagrange stellar–mass black hole to have mass m_3. For the simulated two–body, Single EMRI system comparison we define m_3 to be negligible, but otherwise employ the identical equations and methods. Let G represent the gravitational constant and c be the speed of light. With coordinates (x, y, z), we set each body's position as $\vec{x}_\alpha$, velocity as $\vec{v}_\alpha = \dot{\vec{x}}_\alpha$, and linear momentum as $\vec{p}_\alpha = m_\alpha \cdot \vec{v}_\alpha$ such that $\alpha = 1, 2, 3$ for each body α. This general formulation of the equations of motion would easily allow for additional particles beyond $N = 3$.

The Hamiltonian expansion of our black hole system including the Newtonian (H_0), 1PN (H_1), and dissipative 2.5PN ($H_{2.5}$) terms, is defined as [2], [27], [28], [29]

$$H = H_0 + \frac{1}{c^2} H_1 + \frac{1}{c^4} H_2 + \frac{1}{c^5} H_{2.5}. \tag{3.1}$$

By taking the partial derivative of H, we result in the equations of motion for each black hole α [19], [2], [28], [30]

$$\dot{\vec{x}}_\alpha = \sum_i \frac{\partial H_i}{\partial \vec{p}_\alpha} \tag{3.2}$$

$$\dot{\vec{p}}_\alpha = -\sum_i \frac{\partial H_i}{\partial \vec{x}_\alpha}. \tag{3.3}$$

In the Hamiltonian expansion, the Newtonian term H_0 is given by [16], [2], [29]

$$H_0 = \frac{1}{2}\sum_{\alpha}\frac{|\vec{p}_\alpha|^2}{m_\alpha} - \frac{G}{2}\sum_{\alpha}\sum_{\beta\neq\alpha}\frac{m_\alpha m_\beta}{r_{\alpha\beta}} \tag{3.4}$$

which takes into consideration the gravitational pull of each massed–body. The post-Newtonian equations of motion take general-relativity into account, such that first post-Newtonian (1PN) and second post-Newtonian (2PN) terms introduce different relativistic corrections to the equations of motion. As both the 1PN and 2PN terms conserve energy and angular momentum, but the 2PN includes secondary order terms, we do not include the 2PN term within this paper. However, as the 1PN is the leading order conservative post–Newtonian term, we do account for the 1PN term H_1 defined by [16], [2], [24], [29]

$$\begin{aligned} H_1 = &-\frac{1}{8}\sum_{\alpha} m_\alpha\left(\frac{|\vec{p}_\alpha|^2}{m_\alpha^2}\right)^2 \\ &-\frac{G}{4}\sum_{\alpha}\sum_{\beta\neq\alpha}\frac{1}{r_{\alpha\beta}}\left[6\frac{m_\beta}{m_\alpha}|\vec{p}_\alpha|^2 - 7\vec{p}_\alpha\cdot\vec{p}_\beta - (\vec{n}_{\alpha\beta}\cdot\vec{p}_\alpha)(\vec{n}_{\alpha\beta}\cdot\vec{p}_\beta)\right] \\ &+\frac{G^2}{2}\sum_{\alpha}\sum_{\beta\neq\alpha}\sum_{\gamma\neq\alpha}\frac{m_\alpha m_\beta m_\gamma}{r_{\alpha\beta}r_{\alpha\gamma}} \end{aligned} \tag{3.5}$$

where $r_{\alpha\beta}$ and $\vec{n}_{\alpha\beta}$ are

$$r_{\alpha\beta} = |\vec{r}_{\alpha\beta}| \tag{3.6}$$

$$\vec{n}_{\alpha\beta} = \frac{\vec{r}}{r_{\alpha\beta}} \tag{3.7}$$

such that

$$\vec{r}_{\alpha\beta} = \vec{x}_\alpha - \vec{x}_\beta. \tag{3.8}$$

Considering only the Newtonian and 1PN terms thus far, we test the numerical accuracy of our simulation, showing the three–body system conserves energy and angular momentum. The inclusion of the dissipative 2.5PN term takes into account the system's loss of energy and angular momentum through gravitational radiation emission. To model the inspiral phase of an EMRI system, this term is required. The 2.5PN term is given by [2], [30] [31]

$$H_{2.5} = \frac{G}{45}\chi^{ij}(\vec{x}_\alpha, \vec{p}_\alpha)\dot{\chi}_{ij}(\vec{x}_\alpha, \vec{p}_\alpha) \tag{3.9}$$

where

$$\begin{aligned}\chi_{ij}(\vec{x}_\alpha, \vec{p}_\alpha) = &\sum_\alpha \frac{2}{m_\alpha}(|\vec{p}_\alpha|^2\delta_{ij} - 3p_{\alpha,i})p_{\alpha,j}) \\ &+ \sum_\alpha \sum_{\beta\neq\alpha} \frac{Gm_\alpha m_\beta}{r_\alpha\beta}(3n_{\alpha\beta,i}n_{\alpha\beta,j} - \delta_{ij})\end{aligned} \tag{3.10}$$

and

$$\begin{aligned}\dot{\chi}_{ij}(\vec{x}_\alpha, \vec{p}_\alpha) = &\sum_\alpha \frac{2}{m_\alpha}\left[2(\dot{\vec{p}}_\alpha\cdot\vec{p}_\alpha)\delta_{ij} - 3(\dot{p}_{\alpha i}p_{\alpha j} + p_{\alpha i}\dot{p}_{\alpha j})\right] \\ &+ \sum_\alpha \sum_{\beta\neq\alpha} \frac{Gm_\alpha m_\beta}{r^2_{\alpha\beta}}\,[\,3(\dot{r_{\alpha\beta i}}n_{\alpha\beta j} + n_{\alpha\beta i}\dot{r}_{\alpha\beta j}) \\ &+ (\vec{n_{\alpha\beta}}\cdot\dot{\vec{r}}_{\alpha\beta})(\delta_{ij} - 9n_{\alpha\beta i}n_{\alpha\beta j})\,]\end{aligned} \tag{3.11}$$

such that i, j are the i-th and j-th coordinates of the α-th body, and δ_{ij} represents the Kronecker delta function. With the inclusion of this term, the system no longer conserves energy and angular momentum. We validate the loss of energy by the system in Section 3.3 of this paper.

3.2 Adaptive Runge-Kutta-Fehlberg

In order to approximate the equations of motion, we use the adaptive Runge–Kutta–Fehlberg Order 4/5 (RKF45) numerical integration method [32]. This method uses an order 4/5 embedded Runge-Kutta pair to readjust the step–size at every time–step in order to control error and ensure numerical accuracy within the approximation. As the numerical solution to the equations of motion varies between periods of fast and slow numerical change due to libration of the two stellar–mass black holes and the system's inspiral, the adaptive step–size adjusts for smaller step–sizes with periods of fast change, and larger step–sizes with periods of slow change.

The Runge–Kutta Method is an iterative–method used to approximate the solution of ordinary differential equations using only the initial conditions of a system. The RKF45 method uses the fourth–order Runge–Kutta to approximate the solution while using the fifth–order Runge–Kutta as an error estimator to determine the error produced by the fourth–order method. By setting an error tolerance, the estimator is used to determine the error produced by the current step–size to adjust as needed.

Let us choose an initial time $t(0) = t_0$, a final time t_n with n time–steps, an initial step–size $h > 0$, and a tolerance T. For implementation with our system, let us define the state of the system by $y_i(t_i) = [\vec{x}_{1i}, \vec{x}_{2i}, \vec{x}_{3i}, \vec{p}_{1i}, \vec{p}_{2i}, \vec{p}_{3i}]^T$ such that we define the

function $\frac{dy_i}{dt_i} = f(t_i, y_i)$ as our equations of motion (i.e. eqs. 3.2 and 3.3), where $i = 0, 1, 2, \ldots, n$.

The definition of the fourth–order approximation w_{i+1} is given by

$$w_{i+1} = w_i + h\left(\frac{25}{216}s_1 + \frac{1408}{2565}s_2 + \frac{2197}{4104}s_4 - \frac{1}{5}s_5\right) \tag{3.12}$$

and the fifth–order approximation z_{i+1} is defined as

$$z_{i+1} = z_i + h\left(\frac{16}{135}s_1 + \frac{6656}{12825}s_3 + \frac{28561}{56430}s_4 - \frac{9}{50}s_5 + \frac{2}{55}s_6\right) \tag{3.13}$$

such that

$$s_1 = f(t_i, w_i) \tag{3.14}$$
$$s_2 = f\left(t_i + \frac{1}{4}h, w_i + \frac{1}{4}hs_1\right) \tag{3.15}$$
$$s_3 = f\left(t_i + \frac{3}{8}h, w_i + \frac{3}{32}hs_1 + \frac{9}{32}hs_2\right) \tag{3.16}$$
$$s_4 = f\left(t_i + \frac{12}{13}h, w_i + \frac{1932}{2197}hs_1 - \frac{7200}{2197}hs_2 + \frac{7296}{2197}hs_3\right) \tag{3.17}$$
$$s_5 = f\left(t_i + h, w_i + \frac{439}{216}hs_1 - 8hs_2 + \frac{3680}{513}hs_3 - \frac{845}{4104}hs_4\right) \tag{3.18}$$
$$s_6 = f\left(t_i + \frac{1}{2}h, w_i - \frac{8}{27}hs_1 + 2hs_2 - \frac{3544}{2565}hs_3 + \frac{1859}{4104}hs_4 - \frac{11}{40}hs_5\right) \tag{3.19}$$

where the coefficients in this equation are defined by the Butcher tableau.

Using equations 3.12 and 3.13, the error estimate is then calculated by

$$e_{i+1} = |z_{i+1} - w_{i+1}|. \tag{3.20}$$

This error estimate is then used in a relative error test,

$$\frac{e_{i+1}}{|w_{i+1}|} < T \tag{3.21}$$

comparing the relative error to the set tolerance (T) to determine whether the error produced by the current step–size requires adjustment. Whether the relative error test fails or succeeds, the new step–size h_{new} becomes

$$h_{\text{new}} = 0.9 \cdot h \cdot \left(\frac{T|w_{i+1}|}{e_{i+1}} \right)^{1/5}. \tag{3.22}$$

If the relative error test in eq. 3.21 is successful, the proceeding state y_{i+1} becomes $y_{i+1} = y_i + z_{i+1}$ and the numerical integration process continues with step–size h_{new} for the next step. If the relative error test fails, the current step is repeated, calculating the fourth and fifth–order approximations with h replaced by h_{new} until the relative error test is successful.

The Runge–Kutta–Fehlberg Method (RKF45) is one of the best–known adaptive step–size, one–step method used to accurately approximate the numerical solution of ordinary differential equations. In reference to this study, this numerical integration method approximates the state solution of the equations of motion for the three–body system over time.

3.3 Numerical Validation

In this section, we validate our implementation of the relativistic post–Newtonian terms given a three–body, supermassive black hole system. To do so, we replicate two numerical validation methods from Bonetti, et al. [2].

The first test validates the numerical implementation of the 2.5PN dissipative radiation term in our simulation. We use our three–body equations of motion to simulate a binary system by considering the third mass to be negligible. In this numerical test, we model the binary system's semi–major axis (a) and eccentricity (e), as these Keplerian orbital elements are related to the system's loss of energy and angular momentum due to the inclusion of the 2.5PN term. The semi–major axis and eccentricity are given by the equations

$$a = \left(\frac{2}{R} - \frac{V^2}{G(m_1 + m_2)} \right)^{-1} \tag{3.23}$$

$$e = \sqrt{1 - \frac{h^2}{G(m_1 + m_2)a}}. \tag{3.24}$$

such that

$$R = \sqrt{X^2 + Y^2 + Z^2} \tag{3.25}$$

$$V^2 = \dot{X}^2 + \dot{Y}^2 + \dot{Z}^2 \tag{3.26}$$

$$\vec{h} = (Y\dot{Z} - Z\dot{Y}, Z\dot{X} - X\dot{Z}, X\dot{Y} - Y\dot{X}) \tag{3.27}$$

$$h^2 = \vec{h} \cdot \vec{h} \tag{3.28}$$

where (X, Y, Z) represents the distance between the two bodies with respective cartesian coordinates and $\vec{h} = (h_x, h_y, h_z)$ [33].

We then compare these results to Peters and Mathews [1] first–order coupled orbit–averaged equations for the time derivative of the eccentricity and semi-major axis

$$\dot{a} = -\frac{64G^3}{5c^5}\frac{m_1 m_2(m_1+m_2)}{a^3(1-e^2)^{7/2}}\left(1+\frac{73}{24}e^2+\frac{37}{96}e^4\right) \tag{3.29}$$

$$\dot{e} = -\frac{304G^3}{15c^5}\frac{m_1 m_2(m_1+m_2)}{a^4(1-e^2)^{5/2}}\left(e+\frac{121}{304}e^3\right). \tag{3.30}$$

These equations only include the 2.5PN correction to the Newtonian equations of motion to numerically integrate the orbital evolution of a two–body system. Therefore, for this comparison to the Peters and Mathews orbit–averaged equations, we exclude the 1PN term from the equations of motion to validate our 2.5 post–Newtonian implementation.

To simulate a comparable binary system, we set the system's masses to be $2m_2 = m_1 = 1M_\odot$, the initial semi-major axis $a_0 = 160G(m_1+m_2)/c^2$ (i.e. 160 gravitational radii), and the initial eccentricity $e_0 = 0.1$. Figure 3.1 displays the results of the orbital evolution comparison, demonstrating exact agreement between our simulated equations and the Peters and Mathews numerically integrated equations of semi-major axis and eccentricity. This confirms that our implementation of the 2.5PN dissipative radiation reaction term accurately loses energy and angular momentum, such that the inspiral evolution ultimately leads to a merger of the black hole system.

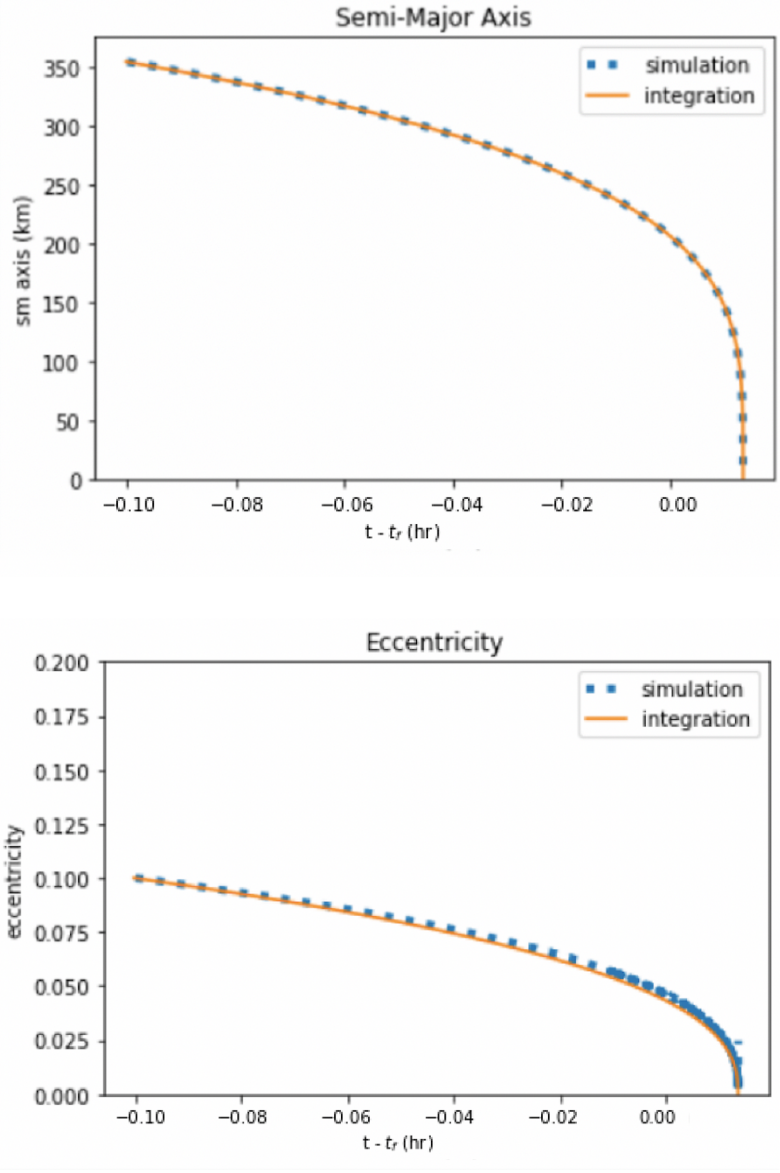

Figure 3.1: The orbital evolution of the semi-major axis and eccentricity of a binary system with masses $2m_2 = m_1 = 1M_\odot$, initial eccentricity $e = 0.1$, and time of merger t_f, considering only the Newtonian and 2.5PN terms in the equations of motion. The blue dotted–curves present our numerically simulated evolution of the system's semi-major axis and eccentricity. The orange curves present the Peters & Mathews [1] orbit–averaged integration of the semi-major axis and eccentricity. Note: this numerical test was confirmed for various initial eccentricities.

For the second validation test, we replicate two figures from Bonetti, et al. shown in Figures S1 and S2 of Appendix A1. We use this validation test to confirm the expected qualitative results of a three–body system with post–Newtonian correction. We construct a hierarchical three–body system with masses $[m_1, m_2, m_3] = [10^9, 3 \cdot 10^8, 5 \cdot 10^8] M_\odot$. The inner binary of this system is comprised of body 1 and body 2 with semi–major axis $a_{\rm in}$ and eccentricity $e_{\rm in}$. The outer binary of this system is defined by body 3 and the center of mass for the inner binary with semi–major axis $a_{\rm out}$ and eccentricity $e_{\rm out}$.

We then model the relative separation, circularity, and inclination of the inner binary in the hierarchical three–body system defined above. The circularity of the inner binary is defined as $1 -$ eccentricity $(1 - e)$ and orbital inclination of the inner binary is calculated using eqs. 3.27 and 3.28 to get [33]

$$I = \arccos \frac{h_z}{h}. \tag{3.31}$$

Figures S1 and S2 from Bonetti, et al. plot the separation, circularity, and inclination of the inner binary of the hierarchical three–body system defined above such that, initially, $a_{\rm in} = 0.44$ pc, $a_{\rm out} = 4.43$ pc, and $e_{\rm out} = 0.5$. The respective initial eccentricities of the inner binary for Figures S1 and S2 are defined as $e_{\rm in} = 0.8$ and $e_{\rm in} = 0$. Figures 3.2 and 3.3 present our replicated results of the inner binary of each hierarchical three–body system. Let us note that the red curve plotted in each separation plot represents the semi-major axis of the inner binary ($a_{\rm in}$).

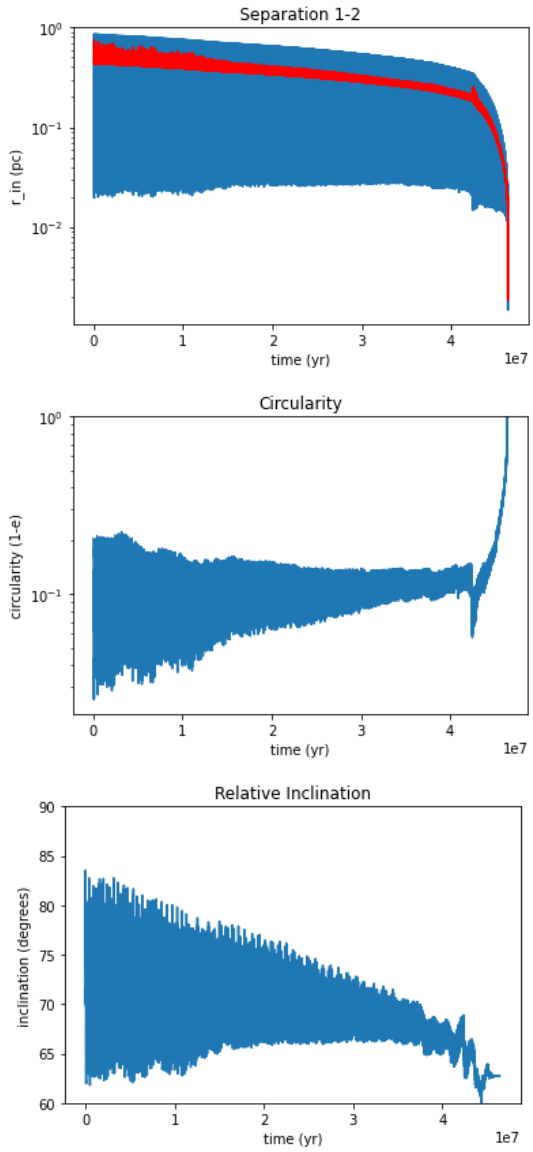

Figure 3.2: The relative separation, circularity, and inclination for the inner binary (constructed of bodies 1 and 2) of a hierarchical three–body black hole system with masses $[m_1, m_2, m_3] = [10^9, 3 \cdot 10^8, 5 \cdot 10^8] M_\odot$. *The initial semi-major axis and eccentricity of the inner and outer binary are set as* $a_{in} = 0.44\ pc, e_{in} = 0.8, a_{out} = 4.43\ pc, e_{out} = 0.5$, *such that the outer binary is constructed of the inner binary center of mass* $(m_1 + m_2)$ *and body 3. The initial relative inclination of the two orbits is* $i = 80°$. *The red curve in the inner binary separation plot represents the evolution of the inner binary's semi-major axis* a_{in}.

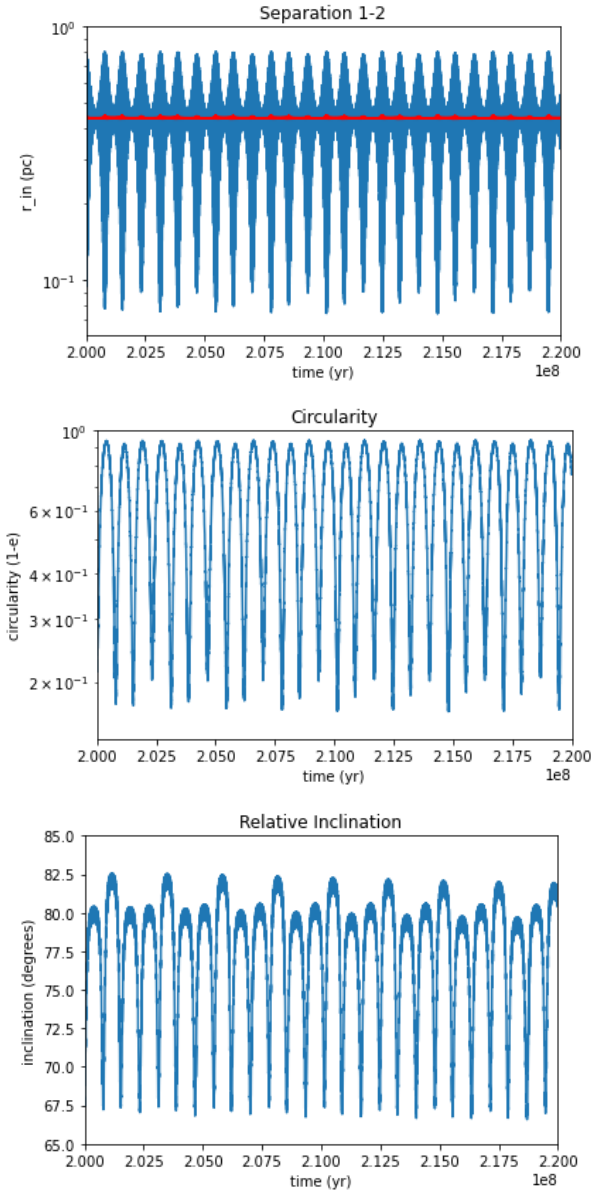

Figure 3.3: The relative separation, circularity, and inclination for the inner binary of a hierarchical three–body black hole system with masses $[m_1, m_2, m_3] = [10^9, 3 \cdot 10^8, 5 \cdot 10^8] M_\odot$. *The initial semi-major axis and eccentricity of the inner and outer binary are set as* $a_{in} = 0.44\ pc, e_{in} = 0, a_{out} = 4.43\ pc, e_{out} = 0.5$ *and the initial relative inclination of the two orbits is* $i = 80°$. *The red curve in the inner binary separation plot represents the evolution of the inner binary's semi-major axis* a_{in}. *Note the different time scale with respect to Figure 3.2: even after* $2 \cdot 10^8$ *yrs, the inner binary has experienced very little evolution.*

Figures 3.2 and 3.3 display differing time scales as the inner binary in Figure 3.2 rapidly merges in approximately $t \sim 4 \cdot 10^7$ years, while the inner binary in Figure 3.3 displays very little evolution even after approximately $t \sim 2 \cdot 10^8$ years. This occurs due to the variability in the respective inner binary's initial eccentricities. With a high initial eccentricity of $e_{\text{in}} = 0.8$ in Figure 3.2, we identify a rapid merger of the inner binary, while a zero initial eccentricity in Figure 3.3 displays very little evolution on a much longer time scale.

Figures 3.2 and 3.3 are qualitatively identical to Figures S1 and S2 from Bonetti, et al. In the respective plots shown in Figures S1 and S2 from Bonetti, et al, they present two variations of numerical precision for each system, finding that the results of the differing numerical precision lead to consistent qualitative behavior, but varying quantitative behavior. From these findings, they determine that the three–body problem is quantitatively dependent upon numerical precision due to its intrinsic chaotic nature. This implies that the quantitative differences found in our resulting Figures 3.2 and 3.3 are due to numerical precision. Let us note that Bonetti, et al. includes the 2PN corrective term to simulate these system, while we do not, which may also act as a factor in our differing quantitative results. Despite these numerical difference, our Figures 3.2 and 3.3 demonstrate identical qualitative behavior compared to Figures S1 and S2 from Bonetti, et al., confirming that our implementation of the post–Newtonian corrections to the equations of motion accurately simulate the expected results.

Provided the results of the two numerical tests presented in this section, we have validated our numerical implementation of the first and 2.5 post–Newtonian corrective terms in the equations of motion of a three–body black hole system. This confirms

that we accurately simulate the expected results of the various systems we present in this paper.

3.4 Quadrupole Formula

In order to accurately capture a system's inspiral evolution within a gravitational wave signal, it is necessary to evaluate the multipole *plus* and *cross* terms of the quadrupole formula [34], as the LISA mission will detect both polarizations of gravitational wave signals [4]. To simulate the gravitational waveform produced by each system, we use the numerically–integrated position of each body ($\vec{x}_\alpha$) to calculate the quadrupole expansion of the gravitational wave field, far from the black hole system.

The quadrupole formula describes the system's leading order gravitational wave emission based on the mass quadrupole moment over time. The quadrupole moment $\mathbf{Q}$ at each time is defined as the sum of $Q_{i,j}$ such that [29], [34], [35], [36], [37]

$$Q_{ij} = \sum_{\alpha} m_\alpha \left(3x_{\alpha,i}x_{\alpha,j} - |\vec{x}_\alpha|^2\delta_{ij}\right) \tag{3.32}$$

over each α–body such that i and j sum over the coordinates (x,y,z) where $\delta_{i,j}$ represents the Kronecker delta function. Taking the second time derivative of the quadrupole moment $Q_{i,j}$, the resulting gravitational wave quadrupole formula is defined as the sum [29], [35], [36], [37]

$$h_{i,j}(t,d) = \frac{2G}{c^4 d}\ddot{\mathbf{Q}}(t - d/c) \tag{3.33}$$

which is a function of time t and the observational distance d. In this work, we do

not specify a distance to the source, but for typical LISA EMRI systems, the distance d will be of the order of $100 - 1000$ Mpc.

The multipole expansion, *plus* and *cross* terms of the quadrupole formula at each time are given by [34]

$$h_{+} = -h_{1,1} \tag{3.34}$$

$$h_{\mathbf{x}} = h_{1,0} \tag{3.35}$$

which model each system's expected gravitational waveform.

Taking the Fast Fourier Transform (FFT) of $h_{+}(t)$ and $h_{\mathbf{x}}(t)$, we determine the power spectrum of each multipole waveform. These individual signals then allow us to calculate the total amplitude of the gravitational waveform over time defined as $\tilde{h}_{\text{tot}}(f)$ from the FFT formula such that

$$\tilde{h}_{\text{tot}} = \sqrt{\tilde{h}_{+}^{2} + \tilde{h}_{\mathbf{x}}^{2}}. \tag{3.36}$$

In Section 4 we use eqs. 3.34, 3.35, and 3.36 to present the amplitude of short–term gravitational wave emissions and simulate the expected signal from LISA using the long–term inspiral waveform.

Chapter 4

Results

In the following section of this paper, we present various Resonant Trojan EMRI systems to identify their unique orbital features and determine whether the LISA mission will find a detectable difference between the gravitational wave signals produced by this system compared to a Single EMRI system. To do so we use the numerically integrated post–Newtonian equations of motion from Section 3.1 to plot various position dynamics and use the quadrupole formula to model gravitational waveforms and their respective amplitude.

In order to visualize the orbital dynamics of each system, we consider a co-rotational frame of reference around the system's center of mass such that the supermassive black hole initially resides in this location. For the following analyses, we define a_0 to be the initial separation of each body to be used as a factor to set each initial position $\vec{x}_\alpha(0)$. The value a_0 is considered in terms of the gravitational radius r_g of the system such that

$$r_g = \frac{G(m_1 + m_2 + m_3)}{c^2}. \tag{4.1}$$

Using this initial separation a_0, the initial orbital period P_0 of each system is defined as

$$P_0 = \sqrt{\frac{4a_0^3\pi^2}{G(m_1 + m_2 + m_3)}}. \tag{4.2}$$

The initial velocity factor v_0 is then given by

$$v_0 = (2\pi a_0)/P_0 \tag{4.3}$$

to set the initial velocity $\dot{\vec{x}}_\alpha(0)$ of each body. These initial velocities are used to set the initial linear momenta $\vec{p}_\alpha(0) = m_\alpha \cdot \dot{\vec{x}}_\alpha(0)$ to calculate eqs. 3.2 and 3.3, i.e. the equations of motion.

Let the initial position of each body be defined as

$$\vec{x}_1(0) = \Big(-(m_2\vec{x}_{2,0} + m_3\vec{x}_{3,0})/m_1, \quad 0, \quad 0\Big) \tag{4.4}$$

$$\vec{x}_2(0) = \Big(a_{2,0}\cos(\lambda_2), \quad a_{2,0}\sin(\lambda_2), \quad 0\Big) \tag{4.5}$$

$$\vec{x}_3(0) = \Big(a_{3,0}\cos(\lambda_3), \quad a_{3,0}\sin(\lambda_3), \quad 0\Big) \tag{4.6}$$

where $a_{2,0}$ and $a_{3,0}$ represent variations to the initial separation a_0 and λ_2, λ_3 represent the initial angle of each body. The initial velocity of each body is then given by

$$\dot{\vec{x}}_1(0) = \Big(0, \quad -(m_2\dot{\vec{x}}_{2,0} + m_3\dot{\vec{x}}_{3,0})/m_1, \quad 0\Big) \tag{4.7}$$

$$\dot{\vec{x}}_2(0) = \Big(-v_0\sin(\lambda_2), \quad v_0\cos(\lambda_2), \quad 0\Big) \tag{4.8}$$

$$\dot{\vec{x}}_3(0) = \Big(-v_0\sin(\lambda_3), \quad v_0\cos(\lambda_3), \quad 0\Big). \tag{4.9}$$

For each system, we redefine $a_{2,0}, a_{3,0}$, and λ_2, λ_3 to simulate differing orbital dynamics of the Resonant Trojan system. Let us note that the changes made to these variables are very minor, as the three–body problem is inherently chaotic in nature and Lagrange's equilibrium configuration produces stable orbital dynamics based on the system's sensitive dependence upon initial condition.

In this section, we first consider a perfectly equilateral configuration of the three bodies in the Resonant Trojan system. Modeling the short–term gravitational waveform of this system, we identify no unique features compared to a Single EMRI

system. We then vary the system's initial conditions to model the two stable orbital dynamic families based on the libration of the two stellar–mass black holes. The short–term gravitational waveforms of each variation exhibit identifiable unique features compared to a Single EMRI system. Lastly, we present a comparison test of the expected gravitational wave signal produced by the inspiral of a circular Single EMRI and equilateral Resonant Trojan EMRI. Based on this test, we determine that the LISA mission will *not* be able to identify a unique signal produced by a perfectly circular Resonant Trojan system in the quadrupole limit [26]. We will discuss this research's future comparison tests to determine whether LISA will be able to detect unique signals from a Resonant Trojan EMRI given various orbital dynamics of the system.

4.1 Fundamental Resonant Trojan EMRI

The Fundamental Resonant Trojan EMRI represents a perfectly equilateral configuration of the three–body system such that the initial positions of the two stellar–mass BHs are the exact analogous locations of Jupiter and the L4 point, with initial conditions $a_{2,0} = a_0, a_{3,0} = a_0, \lambda_2 = 0, \lambda_3 = \pi/3$ where we let $a_0 = 50 \cdot r_g$. We choose to model a $1:1$ mass-ratio of $m_2 : m_3$ such that $(m_1, m_2, m_3) = ([10^5, 10, 10]M_\odot)$. To examine the orbital behavior of this system, we plot only the short–term results of this simulation.

The resulting co–rotational dynamics of this system are shown in Figure 4.1. Based on the perfectly equilateral initial configuration, the two stellar–mass BHs show extremely minimal libration from the analogous stable Jupiter and L4 fixed

points. As these stellar–mass bodies co–rotate counter–clockwise around the SMBH, their lack of libration produces a purely sinusoidal gravitational waveform shown in Figure 4.2.

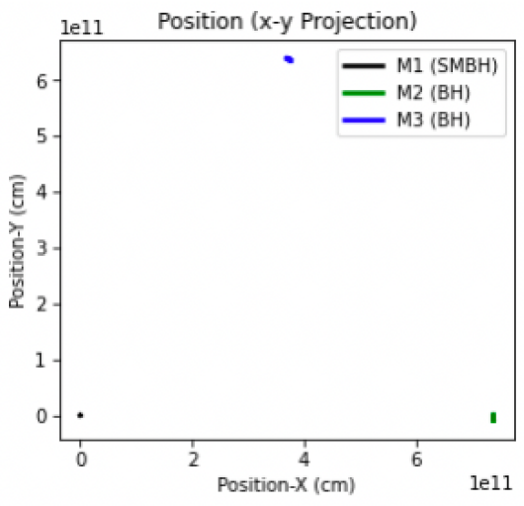

Figure 4.1: The co–rotational dynamics of the Fundamental Resonant Trojan EMRI system in the $x - y$ projection plane. The given initial conditions are $a_{2,0} = a_0, a_{3,0} = a_0, \lambda_2 = 0, \lambda_3 = \pi/3$ where $a_0 = 50 \cdot r_g$, with masses $m_1 = 10^5 M_\odot$ (SMBH) and $m_2 = m_3 = 10 M_\odot$ (1:1 mass ratio M2:M3).

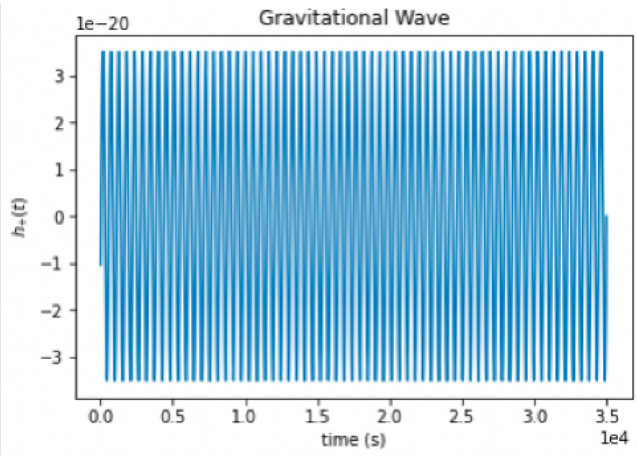

Figure 4.2: The gravitational waveform of the system plotted in Figure 4.1. This system produces a pure sinusoidal waveform, demonstrating an exact match to the gravitational waveform produced by a Single EMRI system.

It is known that at the leading quadrupole order, a non-eccentric Single EMRI system produces a purely sinusoidal gravitational waveform [26], which would exactly match the results shown in Figure 4.2. This implies that the lack of libration from the two stellar–mass BHs, causes the gravitational waveform of the Fundamental Resonant Trojan EMRI system to be indistinguishable from a Single EMRI system. To analyze this result further, we plot the power spectrum of this gravitational waveform in Figure 4.3.

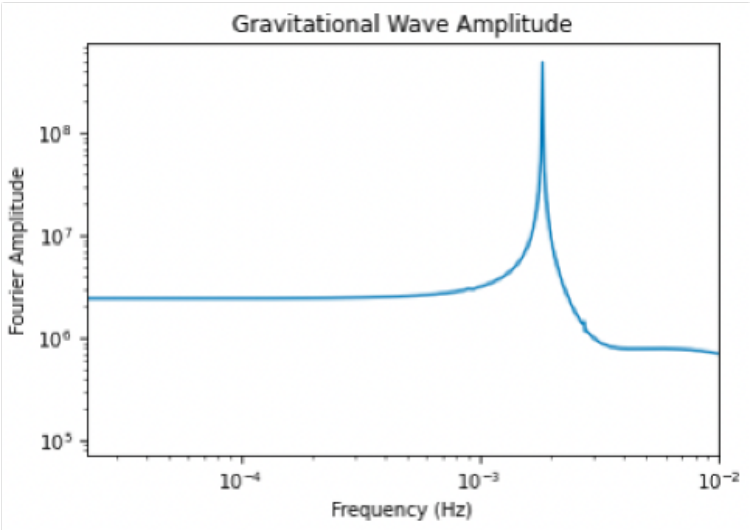

Figure 4.3: The gravitational wave amplitude of the system plotted in Figure 4.1. The single peak shown in this figure occurs at twice the orbital frequency of the system which represents the motion of the two stellar–mass black holes co–rotating around the central, supermassive black hole.

The single peak shown in Figure 4.3 occurs at twice the orbital frequency of the system which represents the motion of the two stellar-mass BHs co–rotating around the central, SMBH. While the motion of a body around the SMBH is detected, there is no indication of three bodies within this system as the relative motion of the two stellar–mass BHs is negligible. This confirms our result from Figure 4.2, that

the short–term gravitational waveform of the Fundamental Resonant Trojan EMRI system is indistinguishable from a Single EMRI system as the system presents no unique features. Let us note that the height of single peak shown in Figure 4.3 informs us of the mass and separation of the detected bodies, and the width displays the libration frequency detected.

Based on the results of the Fundamental Resonant Trojan EMRI system shown in Figures 4.1, 4.2, and 4.3, we conclude that the gravitational waveform produced by this system is identical to the Single EMRI system waveform. This implies the expectation that the system's gravitational wave signal detected from LISA, will be indistinguishable from a Single EMRI system. We present the long–term inspiral evolution of these systems in Subsection 4.4 to simulate LISA's expected signal detection. In the following two Subsections 4.2 and 4.3, we use the results produced by this system from Figures 4.1, 4.2, and 4.3 to represent the resulting orbital dynamics and gravitational waveform of a Single EMRI system, as we have identified no unique features between a Fundamental Resonant Trojan EMRI and Single EMRI system.

4.2 Tadpole Orbital Family

By slightly varying the initial conditions $a_{2,0}, a_{3,0}$, and λ_2, λ_3, the Resonant Trojan system consists of two stable orbital dynamic families based on the libration of the two stellar–mass BHs. The first of these families is known as the Tadpole, or Oval orbital dynamics. The initial conditions presented for the Tadpole family minimally differ from the exact analogous locations of Jupiter and the L4 point such that $a_{2,0} = a_0, a_{3,0} = a_0, \lambda_2 = 0.1, \lambda_3 = \pi/3 - 0.1$ where we let $a_0 = 50 \cdot r_g$. The system's sensitive

dependence to initial conditions is considered to produce this stable orbital dynamic.

We choose to model a $1:1$ mass-ratio of $m_2 : m_3$ such that $(m_1, m_2, m_3) = ([10^5, 10, 10]M_\odot)$. To examine the orbital behavior of this system, we plot only the short–term results of this simulation. The resulting effects of these initial conditions on the co–rotational dynamics of this system can be viewed in Figure 4.4. With this slight change to the initial conditions compared to that of Figure 4.1, we identify a libration of the two stellar-mass BHs from their initial positions, offset from that of the analogous Jupiter and the L4 points in Figure 4.4. This comparison of Figures 4.1 and 4.4 demonstrates the sensitivity of the initial conditions when modeling the position dynamics of Resonant Trojan EMRI systems, but also shows the stability of the triangle configuration. The stellar–mass BHs in this system deviate from their initial positions such that they follow a "tadpole" or ovular orbital shape, such as defined by this dynamical family name.

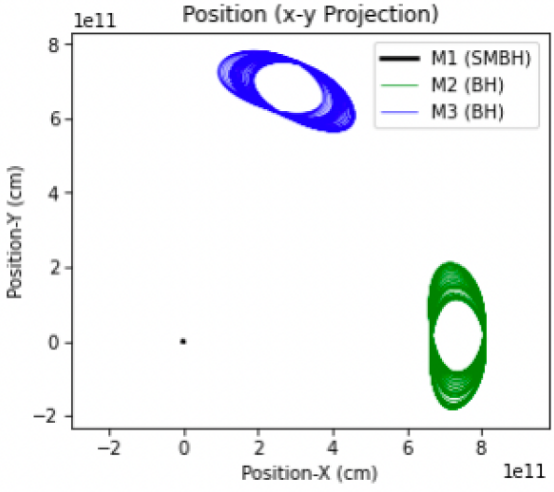

Figure 4.4: The co–rotational tadpole dynamics of the Resonant Trojan EMRI system in the $x-y$ projection plane. The given initial conditions are $a_{2,0} = a_0, a_{3,0} = a_0, \lambda_2 = 0.1, \lambda_3 = \pi/3 - 0.1$ where $a_0 = 50 \cdot r_g$, with masses $m_1 = 10^5 M_\odot$ (SMBH) and $m_2 = m_3 = 10 M_\odot$ (1:1 mass ratio M2:M3). The orbital dynamics of this system exhibit differing libration of the two stellar–mass black holes compared to the Single EMRI system.

The gravitational waveform produced by the Tadpole Resonant Trojan EMRI shown in Figure 4.5, displays identifiable, unique features compared to the purely sinusoidal waveform of the Fundamental Resonant Trojan EMRI, shown in Figure 4.2. This result demonstrates that the tadpole libration of the two stellar–mass BHs affects the waveform of the Resonant Trojan EMRI. Therefore, in the short–term waveform results, the Tadpole Trojan EMRI system is distinguishable from a Single EMRI system.

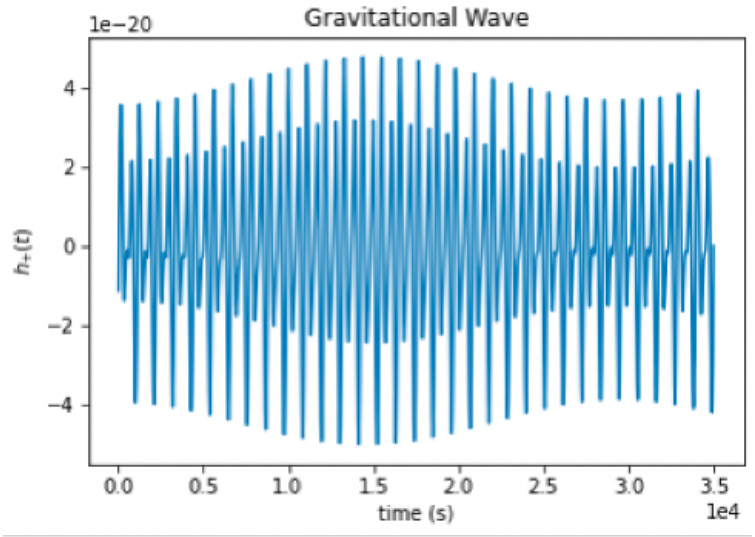

Figure 4.5: The gravitational waveform produced by the Tadpole Resonant Trojan EMRI system in Figure 4.4. This waveform exhibits unique features compared to that of a Single EMRI system.

To analyze this result further, we plot the power spectrum of the Tadpole gravitational waveform in Figure 4.6. The three main peaks presented in Figure 4.6, from left to right, occur at one, two, and three times the orbital frequency of the system. The inner, largest peak at twice the orbital frequency represents the motion of the two stellar-mass BHs co–rotating around the central, SMBH. The two outer peaks at one and three times the system's orbital frequency represent the eccentricity of the

two stellar–mass BHs. The height of each peak shown in Figure 4.6 informs us of the detected bodies, and the width displays the librational frequency detected, such that these two bodies meet at their closest and furthest relative approach at these detected frequencies. It is identified that the width of each peak in Figure 4.6 is greater than the width of the single peak in Figure 4.3.

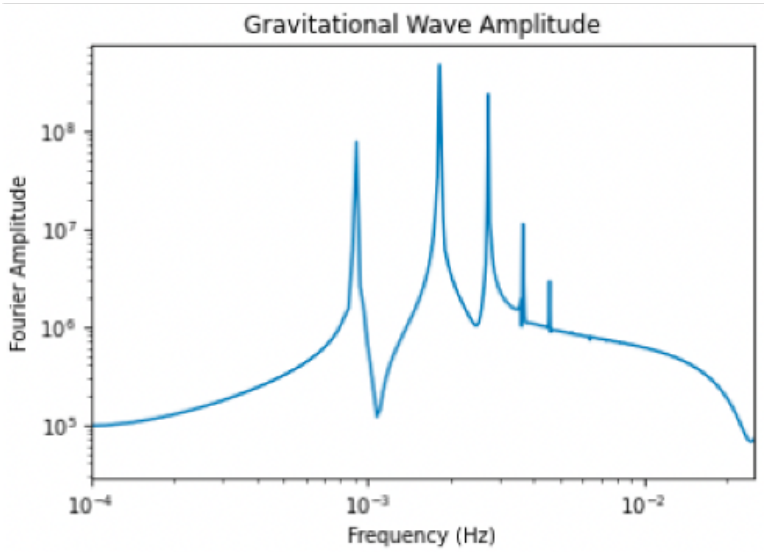

Figure 4.6: The gravitational wave amplitude produced by the Tadpole Resonant Trojan EMRI system in Figure 4.4. The three main peaks presented left to right, occur at one, two, and three times the orbital frequency of the system. The inner, largest peak at twice the orbital frequency represents the relative motion of the two stellar-mass black holes co–rotating around the central, supermassive black hole. The two outer peaks at one and three times the orbital frequency represent the eccentricity of the two stellar–mass black holes.

This analysis of the gravitational wave signal in Figure 4.6 indicates that both the motion around the SMBH and the libration of the two stellar–mass BHs are detected in the gravitational waveforms produced by the Tadpole Resonant Trojan EMRI system. This implies that it is possible to determine whether the source system consists of two or three bodies based on the resulting gravitational waveform. Therefore, in the short–term waveform results, the Tadpole Trojan EMRI system is distinguishable

from a non-eccentric Single EMRI system. We will note that the eccentric signal will also appear in an eccentric Single EMRI system which will be further explored in future work.

In the next subsection 4.3, we model the second stable orbital dynamic family known as the Horseshoe orbits. We also identify the effects of changing another initial condition, the mass–ratio of $m_2 : m_3$, which was not adjusted in our tadpole dynamic analysis.

4.3 Horseshoe Orbital Family

The Horseshoe orbital dynamic family represents the second stable orbital dynamic system produced by the Lagrange solution. The Horseshoe Resonant Trojan EMRI system minimally differs from the Fundamental and Tadpole Trojan EMRI system such that its initial conditions are given by $a_{2,0} = 1.01 \cdot a_0, a_{3,0} = 0.99 \cdot a_0, \lambda_2 = 0.01, \lambda_3 = \pi/3 - 0.01$ where we let $a_0 = 50 \cdot r_g$.

In this horseshoe dynamic analysis, we choose to model three mass–ratios of $m_2 : m_3$ to display the orbital adjustments made by changing the mass of each body. We first choose to model a $1 : 1$ mass-ratio of $m_2 : m_3$ such that $(m_1, m_2, m_3) = ([10^5, 10, 10]M_\odot)$. The resulting effects of these initial conditions on the co–rotational dynamics of this system can be viewed in Figure 4.7.

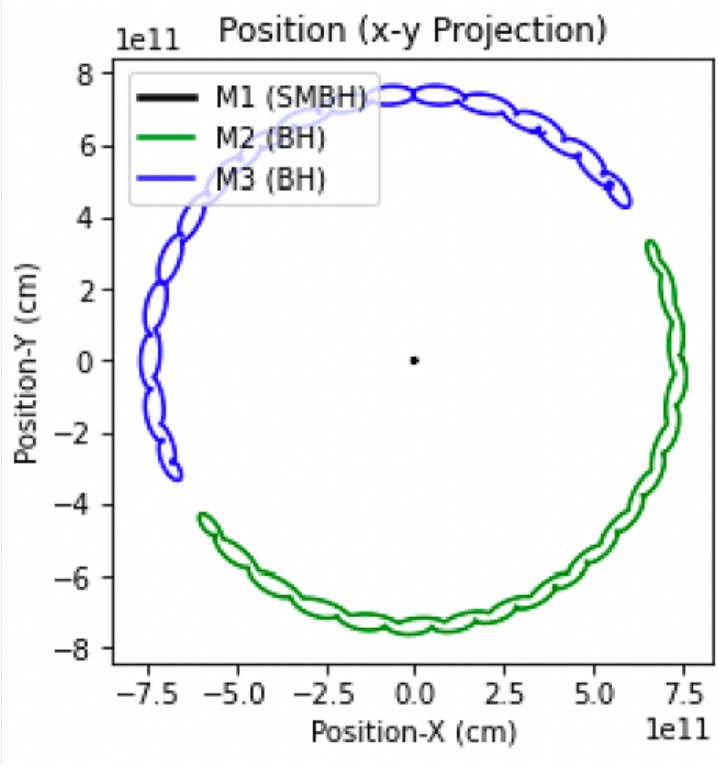

Figure 4.7: The co–rotational horseshoe dynamics of the Resonant Trojan EMRI system in the $x - y$ projection plane. The given initial conditions are $a_{2,0} = 1.01 \cdot a_0, a_{3,0} = 0.99 \cdot a_0, \lambda_2 = 0.01, \lambda_3 = \pi/3 - 0.01$ where $a_0 = 50 \cdot r_g$, with masses $m_1 = 10^5 M_\odot$ (SMBH) and $m_2 = m_3 = 10 M_\odot$ (1:1 mass ratio M2:M3). The orbital dynamics of this system exhibit differing libration of the two stellar–mass black holes compared to the Single EMRI and Tadpole Resonant Trojan EMRI systems.

With this slight change to the system's initial conditions compared to that of Figures 4.1 and 4.4, we identify a major change in the libration of the two stellar-mass BHs from both the Fundamental and Tadpole Resonant Trojan EMRIs. This demonstrates the sensitivity of the initial conditions when modeling the position dynamics of Resonant Trojan EMRI systems. Figure 4.7 demonstrates the orbital behavior of this system such that the two stellar–mass BHs deviate from their offset analogous Jupiter and the L4 points initial positions such that they follow a "horseshoe" orbital shape. While co–rotating around the central SMBH, the two stellar–mass BHs be-

ginning at their initial positions, horseshoe down to the bottom left hand corner of the plot where they meet at their first closest approach. The stellar–mass BHs then horseshoe back around to the upper right hand corner of the plot where they meet at their second closest approach.

By varying the masses of the two stellar–mass BHs in such a system, we also identify the differing orbital dynamics produced by this change in initial condition. We choose to model the horseshoe dynamics produced by a $2:1$ mass-ratio of $m_2 : m_3$ such that $(m_1, m_2, m_3) = ([10^5, 10, 5]M_\odot)$ and a $3:1$ mass-ratio of $m_2 : m_3$ such that $(m_1, m_2, m_3) = ([10^5, 10, 10/3]M_\odot)$. The resulting $x - y$ projection plane of these varying mass–ratio systems are shown in Figure 4.8 such that the top panel displays the $2:1$ mass–ratio and the bottom panel presents the $3:1$ mass–ratio of the Horseshoe Resonant Trojan EMRI system.

Based on the varying mass–ratio of each system, there is an identifiable difference between Figure 4.7 and both panels of Figure 4.8. Due to the $1:1$ mass–ratio in Figure 4.7, the gravitational effect of each stellar-mass BH are equivalent, causing the width and length of each stellar-mass BH's horseshoe orbital dynamics to be equivalent. The $2:1$ mass–ratio shown in the top panel of Figure 4.8 visualizes the gravitational effect of stellar–mass BH m_2 being twice that of stellar–mass BH m_3. The gravitational effect of each stellar–mass BH adjusts the resulting horseshoe dynamics such that the width and length of orbital path taken by BH m_3 is twice that of BH m_2. The $3:1$ mass–ratio shown in the bottom panel of Figure 4.8 then visualizes the gravitational effect of stellar–mass BH m_2 being three times that of stellar–mas BH m_3. This gravitational effect adjusts the horseshoe dynamics of each stellar–mass BH such that the width and length of orbital path taken by BH m_3 is

three times that of BH m_2. An identical effect is seen in the orbits of Saturn's moons Epimetheus and Janus which roughly have a $3:1$ mass-ratio.

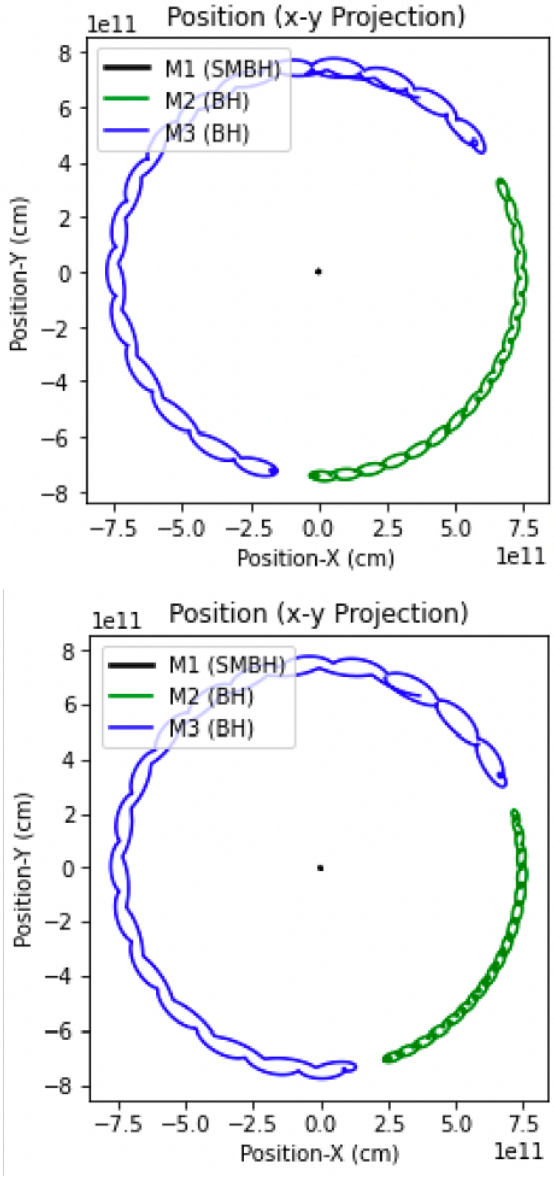

Figure 4.8: The co–rotational horseshoe dynamics of the Resonant Trojan EMRI system in the $x-y$ projection plane. The given initial conditions of each panel are the same as Figure 4.7. The top panel consists of a 2:1 mass ratio of M2:M3 with masses $m_1 = 10^5 M_\odot$ (SMBH) and $m_2 = 2m_3 = 10M_\odot$. The bottom panel consists of a 3:1 mass ratio of M2:M3 with masses $m_1 = 10^5 M_\odot$ (SMBH) and $m_2 = 3m_3 = 10M_\odot$.

As we have increased the mass-ratio of $m_2 : m_3$ throughout Figure 4.7 and each panel of Figure 4.8, the width and length of the orbital dynamics taken by each stellar–mass BH have been adjusted based on the gravitational effect of m_2 and m_3. This implies that the stellar–mass BH orbital features are related to the mass–ratio of $m_2 : m_3$ such that this trend continues to occur for various adjustments to the mass–ratio. While not visualized in this paper, the same orbital trend will occur if the mass–ratio is adjusted for the Tadpole orbital family.

This overall analysis of the Resonant Trojan EMRI horseshoe orbital dynamics presents identifiable unique orbital features compared to that of the Fundamental and Tadpole Resonant Trojan EMRI systems. To further analyze the effects of the Horseshoe Resonant Trojan EMRI initial conditions, we model the gravitational waveform of the $2 : 1$ mass–ratio Horseshoe Resonant Trojan EMRI shown in Figure 4.9.

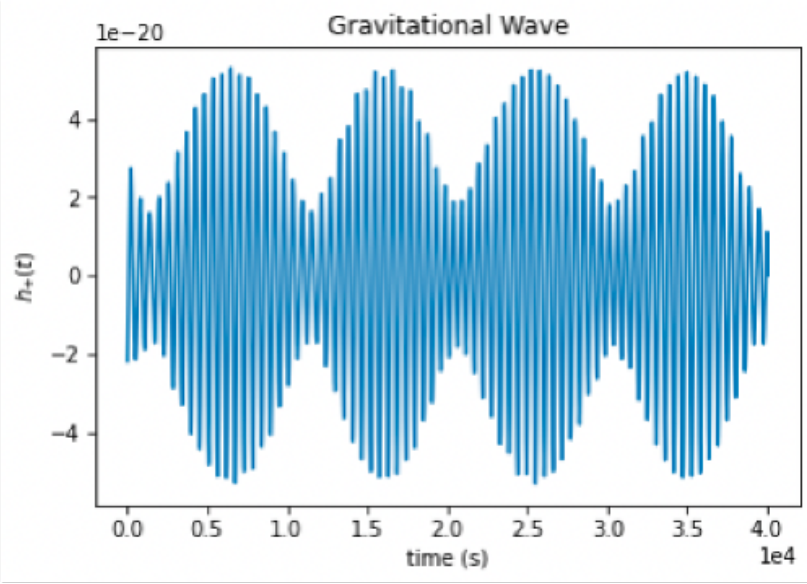

Figure 4.9: The gravitational waveform produced by the Horseshoe Resonant Trojan EMRI system from the top panel of Figure 4.8 with a $2 : 1$ *mass-ratio of M2:M3. This waveform exhibits unique features compared to the Tadpole Resonant Trojan and Single EMRI systems.*

The gravitational waveform produced by the Horseshoe Resonant Trojan EMRI shown in Figure 4.9, displays identifiable, unique features compared to the purely sinusoidal waveform of the Fundamental Resonant Trojan EMRI, shown in Figure 4.2. This result demonstrates that the horseshoe libration of the two stellar–mass BHs affects the waveform of the Resonant Trojan EMRI. Therefore, in the short–term waveform results, the Horseshoe Trojan EMRI system is distinguishable from a Single EMRI system.

This gravitational waveform presented in Figure 4.9 also displays identifiable, unique features compared to the gravitational waveform of the Tadpole dynamic Resonant Trojan EMRI, shown in Figure 4.5. This result demonstrates that not only is there distinguishable difference between the librated and Fundamental Resonant Trojan EMRI systems, but there is also an identifiable difference between the gravitational waveform of the two stable libration dynamics of the Resonant Trojan EMRI, i.e. between the Tadpole and Horseshoe orbital dynamic systems. Therefore, based on the short–term gravitational waveform produced by a Resonant Trojan EMRI, we are able to determine the type of orbital path taken by the two stellar–mass BHs in a system.

To analyze this result further, we present the amplitude of the Horseshoe gravitational waveform shown in Figure 4.10. The three main peaks presented in Figure 4.10, from left to right, occur at one, two, and three times the orbital frequency of the system, just as discussed for the Tadpole gravitational waveform shown in Figure 4.5. In Figure 4.9, the inner, largest peak at twice the orbital frequency represents the motion of the two stellar-mass BHs co–rotating around the central, SMBH.

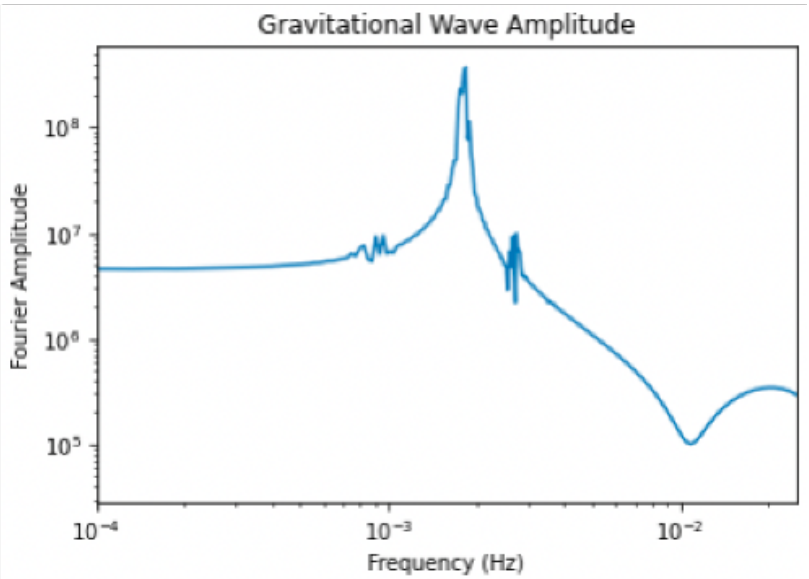

Figure 4.10: The gravitational wave amplitude produced by the Horseshoe Resonant Trojan EMRI system from the top panel of Figure 4.8 with a $2:1$ *mass-ratio of M2:M3. The three main peaks presented left to right, occur at one, two, and three times the orbital frequency of the system. The inner, largest peak at twice the orbital frequency represents the motion of the two stellar-mass black holes co–rotating around the central, supermassive black hole. The two outer peaks at one and three times the orbital frequency represent the non–circular nature of the orbits. The width of the main peak represents the libration frequency.*

The three peaks in Figure 4.10 indicate that both the motion around the SMBH and the eccentricity of the two stellar–mass BHs are detected in the gravitational waveforms produced by the Horseshoe Resonant Trojan EMRI system. Just as discussed for the Tadpole gravitational waveform, this implies that the source of this waveform consists of three bodies. Therefore, in the short–term waveform results, the Horseshoe Resonant Trojan EMRI system is distinguishable from a non-eccentric Single EMRI system. We will note that the eccentric signal will also appear in an eccentric Single EMRI system which will be further explored in future work.

The height of each peak shown in Figure 4.10 informs us of the detected bodies, and the width of the main peak represents the libration frequency. The two outer

peaks at one and three times the orbital frequency represent the non–circular nature of the orbits. It is identified that the width of each peak in Figure 4.10 differ from the peaks presented in Figure 4.6 for the Tadpole Resonant Trojan EMRI system. This confirms our previous result that there is an identifiable difference between the Tadpole and Horseshoe libration dynamics of the Resonant Trojan EMRI system.

This analysis of the Horseshoe Resonant Trojan EMRI presents a variety of orbital features and gravitational waveform results. We have further demonstrated the sensitivity of initial conditions when modeling the position dynamics of Resonant Trojan EMRI by comparing the Horseshoe results to the Fundamental and Tadpole Resonant Trojan EMRI systems. We have also shown that by adjusting the mass–ratio of $m_2 : m_3$ in a Resonant Trojan EMRI system, the width and length of orbital path taken by m_2 and m_3 are related to this mass–ratio. Through this analysis, we have concluded that the Horseshoe orbital dynamics display identifiable unique features compared to that of the Fundamental and Tadpole Resonant Trojan EMRI systems. These orbital dynamics conclude that in short–term waveform results, the Horseshoe Trojan EMRI system is distinguishable from both a non-eccentric Single EMRI and a Tadpole Resonant Trojan EMRI, such that we are able to determine the type of orbital path taken by the two stellar–mass BHs based on the resulting gravitational waveform.

4.4 Single EMRI Gravitational Wave Test

In this final subsection of our results, we determine whether the LISA mission will find a detectable difference between the gravitational wave signals produced by the Fundamental Resonant Trojan EMRI system compared to a Single EMRI system considering the long–term evolution. Based on the results of the Fundamental Resonant Trojan EMRI system shown in Figures 4.1, 4.2, and 4.3 of Subsection 4.1, we concluded that the short–term gravitational waveform produced by this system is identical to a Single EMRI system waveform. This previous analysis implied the expectation that the Fundamental Resonant Trojan EMRI system's gravitational wave signal detected from LISA, will be indistinguishable from a Single EMRI system given non–eccentric orbits. We present the long–term inspiral evolution of these two systems due to gravitational radiation emission to simulate LISA's expected signal detection.

To model each system, we set their initial conditions to be $a_{2,0} = a_{3,0} = a_0, \lambda_2 = 0, \lambda_3 = \pi/3$ where we let $a_0 = 30 \cdot r_g$ such that their initial separation is closer to the ultimate merger of the given bodies to model the inspiral evolution of these two systems before merger. For the Fundamental Resonant Trojan EMRI we set the system's masses to have a $1:1$ mass-ratio of $m_2 : m_3$ such that $(m_1, m_2, m_3) = ([10^5, 10, 10]M_\odot)$. To construct the Single EMRI system, we set $m_1 = 10^5 M_\odot$, $m_2 = \sqrt{3} \cdot 10 M_\odot$, and m_3 to have negligible mass to replicate a two–body system. Calculating the gravitational waveform of each system, we present their resulting amplitudes in Figure 4.11.

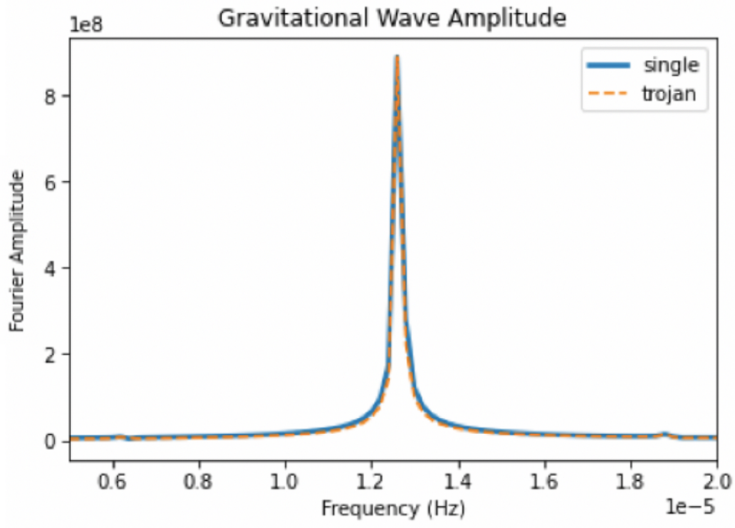

Figure 4.11: The gravitational wave amplitude of the Fundamental Resonant Trojan EMRI system and Single EMRI system given $a_{2,0} = a_0, a_{3,0} = a_0, \lambda_2 = 0, \lambda_3 = \pi/3$ *where* $a_0 = 30 \cdot r_g$*. The Fundamental Resonant Trojan EMRI has masses* $m_1 = 10^5 M_\odot$ *(SMBH) and* $m_2 = m_3 = 10 M_\odot$ *(1:1 mass ratio M2:M3). The Single EMRI system has masses* $(m_1, m_2, m_3) = [10^5, \sqrt{3} \cdot 10, 0] M_\odot$*. The single peak shown in this figure occurs at twice the orbital frequency of each system which represents the motion of the stellar-mass black hole(s) co–rotating around the central, supermassive black hole. The initial velocity of* m_2 *in the Single EMRI system is adjusted slightly from the Fundamental Resonant Trojan EMRI* m_2 *to compensate for the differing total masses of these systems. This result displays numerically close agreement between the Fundamental Resonant Trojan EMRI and Single EMRI systems' gravitational wave amplitude.*

The resulting gravitational wave amplitude of the Fundamental Resonant Trojan EMRI and Single EMRI systems in Figure 4.11 display numerically close agreement in frequency, height, and width. This demonstrates that the gravitational waveforms produced by the non–eccentric Fundamental Resonant Trojan EMRI and Single EMRI systems are indistinguishable. Let us note that given the presented initial conditions, the resulting gravitational waveforms produced identical quantitative signals, with differing amplitude height. This is due to the varying masses of the two systems,

causing a difference in orbital period and initial velocity. In order to closely match the frequency of each system, as shown in Figure 4.11, the initial velocity of the Single EMRI system was adjusted to compensate for the differing total masses of these systems using the chirp mass formula from Asada [26].

Given the results shown in Figure 4.11, if this non–eccentric Fundamental Resonant Trojan EMRI were detected from the LISA mission, the signal would show a Single EMRI system with $\sqrt{3}$ times the mass of the stellar–mass BH (m_2) and $\sqrt{3}$ times as far away from LISA's detection site. This is because the combined mass of the stellar–mass BHs (m_2 and m_3) in the Fundamental Resonant Trojan EMRI would be double that of the Single EMRI system's stellar–mass BH (m_2), and only the motion of a stellar–mass BH around the SMBH is detected. If we somehow knew the distance from the merger, this degeneracy could be broken.

To further analyze the results from Figure 4.11, we simulate the signals expected from LISA's detection for each system. To do so, we calculate the gravitational wave amplitude of each system given various initial separations up to merger. We then combine these separation amplitudes and their frequencies into a contour plot of the gravitational wave normalized amplitude throughout the long–term inspiral evolution of each system.

This process will produce the characteristic gravitational wave signal "chirp" expected from LISA's detection. This chirp refers to the increasing frequency and amplitude of a system due to the loss of energy and angular momentum of the inspiral evolution up to merger. The result of these simulations are presented in Figures 4.12 and 4.13 such that Figure 4.12 displays the Single EMRI signal and Figure 4.13 shows the Fundamental Resonant Trojan EMRI signal.

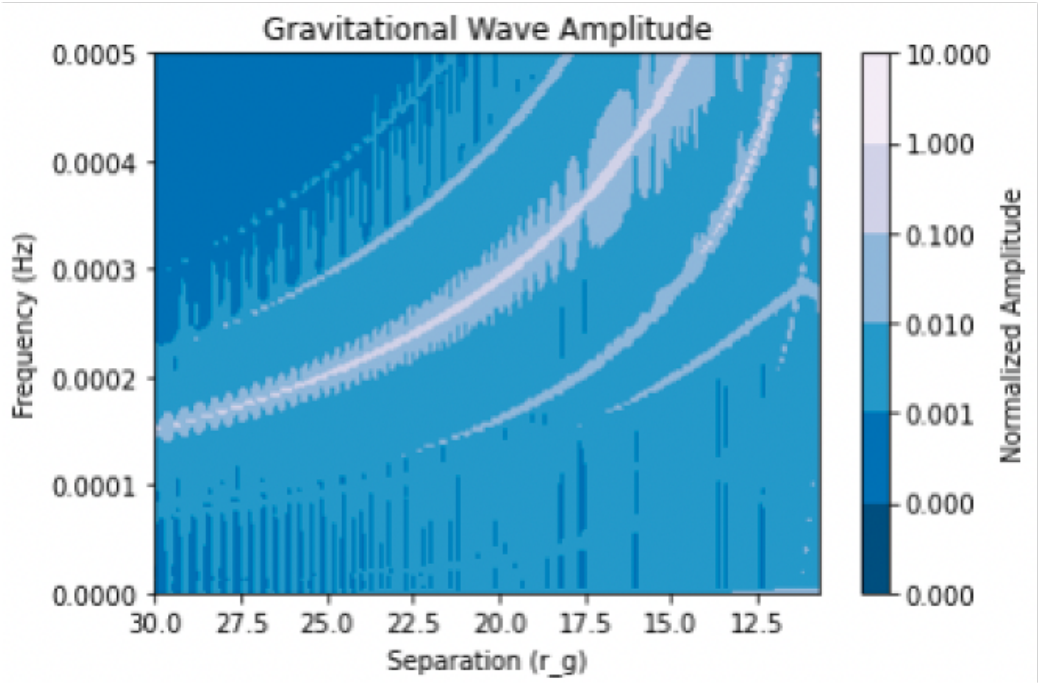

Figure 4.12: The gravitational wave normalized amplitude contour map of the Single EMRI system given $a_{2,0} = a_0, a_{3,0} = a_0, \lambda_2 = 0, \lambda_3 = \pi/3$ with various initial separations a_0 in terms of the gravitational radius r_g. The masses of this system are defined as $(m_1, m_2, m_3) = [10^5, 10, 0]M_\odot$. This plot simulates the expected LISA signal given the inspiral evolution up to merger. Note that the initial velocity used to produce this plot corresponds to the Keplerian circular orbit, which is slightly eccentric in 1PN. The frequency axis in this figure demonstrates that this system inspiral falls within the LISA detectable frequency band. This expected signal is nearly indistinguishable from that of the Fundamental Resonant Trojan EMRI system in Figure 4.13.

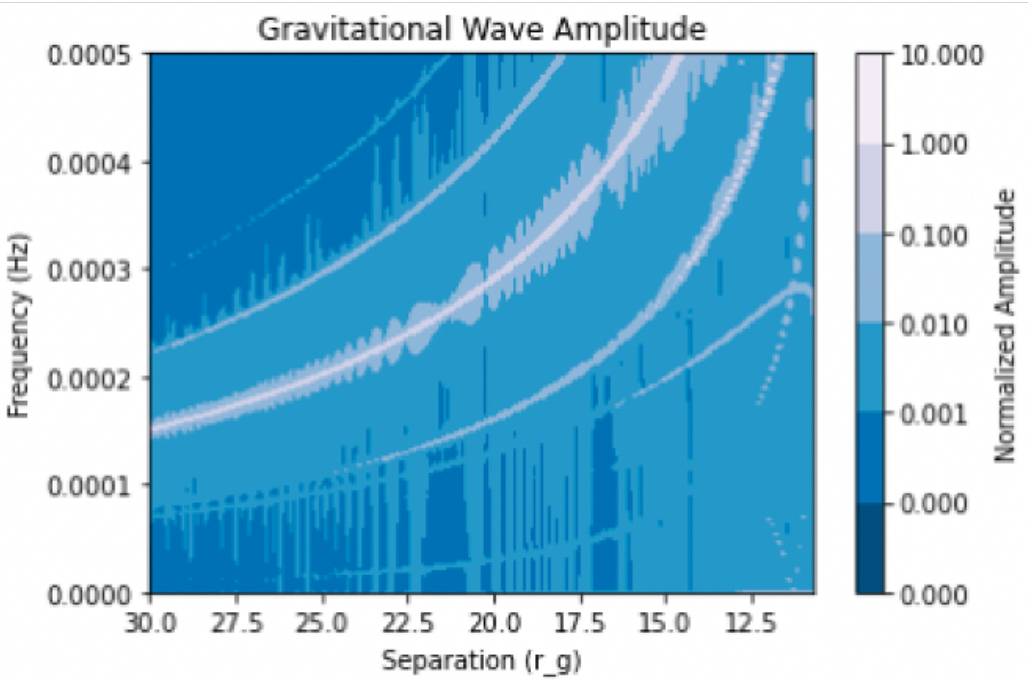

Figure 4.13: The gravitational wave amplitude contour map of the Fundamental Resonant Trojan EMRI system given $a_{2,0} = a_0, a_{3,0} = a_0, \lambda_2 = 0, \lambda_3 = \pi/3$ with various initial separations a_0 in terms of the gravitational radius r_g. The masses of this system are $m_1 = 10^5 M_\odot$ (SMBH) and $m_2 = m_3 = 10 M_\odot$ (1:1 mass ratio M2:M3). Note that the initial velocity used to produce this plot corresponds to the Keplerian circular orbit, which is slightly eccentric in 1PN. This plot simulates the expected LISA signal given the inspiral evolution up to merger. The frequency axis in this figure demonstrates that this system inspiral falls within the LISA detectable frequency band. This expected signal is nearly indistinguishable from that of the Single EMRI system in Figure 4.12.

Figure 4.12 and 4.13 display nearly imperceptible differences in their normalized expected signals from the LISA mission based on their inspiral evolution up to merger. Let us note that the gradual increase of frequency and amplitude shown in these plots demonstrates each system's loss of energy such that energy loss rate is proportional to the square of the gravitational wave amplitude.

To produce each of these of these plots we use an initial velocity that corresponds to the Keplerian circular orbit, which is slightly eccentric in 1PN. Due to this slight eccentricity, we identify four main signals detected. From top to bottom, the first three signals occur at three, two, and one times the orbital frequency of the system over the inspiral evolution. The main signal detected (second signal from the top) that occurs at two times the orbital frequency represents the motion of the stellar–mass BH(s) around the SMBH in each of these EMRI systems. The fourth main signal, located fourth down in each figure, represents the systems' radial frequency evolution such that the "hook" right before merger is a common feature of general relativity.

Lastly, we note that the frequency range shown in Figures 4.12 and 4.13 demonstrate that these system inspirals fall within the LISA detectable frequency band. This implies that both Single and Resonant Trojan EMRI systems will be detectable from the LISA mission.

Based on the nearly identical results shown in Figures 4.12 and 4.13, this source comparison test determines that the LISA mission will *not* be able to identify a unique signal produced by a non-eccentric Fundamental Resonant Trojan system compared to the signal produced by a non-eccentric Single EMRI system. In practice, eccentricity will shrink for the Single EMRIs, but grow for the Trojan EMRIs. In the next section,

we discuss this research's future planned comparison tests to determine whether LISA will be able to detect unique signals from a Resonant Trojan EMRI given various stable orbital dynamics of the system.

Chapter 5

Conclusion

Within the natural world, three–body systems have shown to be abundant amongst various planet and star systems. Based on our observation of three–body systems within the universe, the question remains whether a three–body black hole system will be detected. Through electromagnetic observation, two possible three–body black hole system candidates have been identified. The first being a triple quasar [38] and the second being an electromagnetic (EM) counterpart to a binary black hole merger [39].

More specifically, orbital resonance has been shown to be a common feature amongst these three–body systems [28]. For example, within our own solar system resonant relations occur between bodies such as in the Earth–Moon, Saturn–Moon, and Jupiter–Trojan asteroid systems. In this thesis, we discuss an analogous Jupiter–Trojan black hole system known as the Resonant Trojan EMRI system. We use this system to determine whether the LISA mission will be able to detect a three–body black hole system.

In this thesis, we use the numerically–integrated post–Newtonian equations of motion and quadrupole formula to accurately model the effects of general relativity on the Resonant Trojan EMRI system to gain the best understanding of what a real–world example would look like if the LISA mission were to receive a gravitational signal from a Resonant Trojan EMRI system. We first consider a perfectly equilateral configuration of the three bodies in the Resonant Trojan system. Modeling the short–term gravitational waveform of this system, we identify no unique features compared to a Single EMRI system. We then vary the system's initial conditions to model the two stable orbital dynamic families of the Lagrange solution based on the libration of the two stellar–mass black holes. These stable solutions are known as the Tadpole

and Horseshoe orbital dynamic families. The short–term gravitational waveforms of each variation produce identifiable, unique features compared to a Single EMRI system. Lastly, we present a comparison test of the expected gravitational wave signal produced by the inspiral evolution of a non-eccentric, Single EMRI and equilateral Resonant Trojan EMRI. Based on this test, we determine that the LISA mission will *not* be able to identify a unique signal produced by a non-eccentric Resonant Trojan EMRI system because the signal will appear identical to a Single EMRI system.

In the future of this research, we will further explore the expected LISA signals produced by various orbital dynamics of the Resonant Trojan EMRI system in comparison to the Single EMRI system. As EMRIs are typically captured in highly eccentric orbits [10], we will investigate the inspiral evolution effects of various mass–ratios, eccentricities, and non-planar orbits of the Resonant Trojan EMRI system. We will also explore the two stable orbital dynamics of the Tadpole and Horseshoe Resonant Trojan EMRIs in comparison to the Single EMRI system. As two previous papers from Torigoe, et al. [3] and Asada [26] have demonstrated that the Resonant Trojan EMRI system *is* distinguishable from a Single EMRI system when using the octupole formula to model gravitational wave emissions, we will also expand our use of the qadrupole formula to include the octupole formula to confirm their found results. If we can independently determine the distance d to the merger, then the chirp mass and the total mass can be determined.

As LISA's detection will contain thousands of overlapping gravitational wave signals, the mission's search algorithm uses a "matching" filter to extract merger event signals [27]. This algorithm matching filter uses a collection of gravitational waveform "templates" containing all possible detection events and their possible param-

eters produced by theoretical research [27], such as this work. This collection of waveform templates will allow the LISA mission to optimize the sensitivity of its searching algorithm to extract specific signals amongst the detectors noise, measure the properties of the gravitational source, and present statistical confidence in its detection [8], [21], [9], [14]. Due to this template matching technique, LISA relies heavily on the accuracy of detection templates, as the inaccuracy of these models could lead to missed detections [27], [14]. Thus far, LISA templates have only been produced for *single* EMRI systems [27], displaying an important need for multiple EMRI waveform templates. If unique signals from multiple EMRI systems are detectable, without their template inclusion the LISA mission may not detect these event signals. Therefore, the further exploration of the Resonant Trojan EMRI system is crucial to LISA detection of multiple EMRI systems.

By producing anticipated waveform signals, this work assists in interpreting the future received signals from the LISA mission. Through our theoretical gravitational wave signals, we hope to identify not only how many bodies are within a system, but also what the orbital dynamics of these bodies looked like throughout the inspiral before merger. This research will continue to teach us about the different types of orbital dynamics possible with the Resonant Trojan EMRI system and continue to provide us with more information about the relativistic three–body problem. If we do detect Trojan EMRIs, it will provide strong evidence that these systems form in the accretion disk around the SMBH, but like Jupiter's Trojans, they may be captured dynamically. Overall, studying these Resonant Trojan dynamics and gravitational wave signals will ultimately assist in our understanding of the structure and curvature of space-time around EMRI systems.

Bibliography

[1] P. C. Peters and J. Mathews. Gravitational Radiation from Point Masses in a Keplerian Orbit. *Physical Review*, 131(1):435–440, July 1963. Publisher: American Physical Society.

[2] M. Bonetti, F. Haardt, A. Sesana, and E. Barausse. Post-Newtonian Evolution of Massive Black Hole Triplets in Galactic Nuclei: I. Numerical Implementation and Tests. *Monthly Notices of the Royal Astronomical Society*, 461(4):4419–4434, Oct. 2016. arXiv: 1604.08770.

[3] Y. Torigoe, K. Hattori, and H. Asada. Gravitational waveforms for 2- and 3-body gravitating systems. *Physical Review Letters*, 102(25):251101, June 2009. arXiv: 0906.1448.

[4] P. Amaro-Seoane, et al. Laser Interferometer Space Antenna. Technical report, Feb. 2017. Publication Title: arXiv e-prints ADS Bibcode: 2017arXiv170200786A Type: article.

[5] eLISA Consortium, et al. The Gravitational Universe. Technical report, May 2013. Publication Title: arXiv e-prints ADS Bibcode: 2013arXiv1305.5720E Type: article.

[6] D. V. Martynov, et al. The Sensitivity of the Advanced LIGO Detectors at the Beginning of Gravitational Wave Astronomy. *Physical Review D*, 93(11):112004, June 2016. arXiv: 1604.00439.

[7] S. A. N. Leiva. A Review of the LISA and eLISA Projects. page 4.

[8] J. R. Gair, M. Hewitson, A. Petiteau, and G. Mueller. Space-based Gravitational Wave Observatories. Technical report, Jan. 2022. Publication Title: arXiv e-prints ADS Bibcode: 2022arXiv220110593G Type: article.

[9] E. Barausse, et al. Prospects for fundamental physics with LISA. *General Relativity and Gravitation*, 52:81, Aug. 2020. ADS Bibcode: 2020GReGr..52...81B.

[10] M. Bonetti and A. Sesana. Gravitational wave background from extreme mass ratio inspirals. *Physical Review D*, 102(10):103023, Nov. 2020. arXiv: 2007.14403.

[11] S. Babak, J. Gair, A. Sesana, E. Barausse, C. F. Sopuerta, C. P. L. Berry, E. Berti, P. Amaro-Seoane, A. Petiteau, and A. Klein. Science with the space-based interferometer LISA. V. Extreme mass-ratio inspirals. *Physical Review D*, 95:103012, May 2017. ADS Bibcode: 2017PhRvD..95j3012B.

[12] K. J. Rhook and J. S. B. Wyithe. Realistic Event Rates for Detection of Supermassive Black Hole Coalescence by LISA. *Monthly Notices of the Royal Astronomical Society*, 361(4):1145–1152, Aug. 2005. arXiv: astro-ph/0503210.

[13] K. Destounis and K. D. Kokkotas. Gravitational-wave glitches: resonant islands and frequency jumps in non-integrable extreme-mass-ratio inspirals. *Physical Review D*, 104(6):064023, Sept. 2021. arXiv: 2108.02782.

[14] J. D. Schnittman. Spin-Orbit Resonance and the Evolution of Compact Binary Systems. *Physical Review D*, 70(12):124020, Dec. 2004. arXiv: astro-ph/0409174.

[15] H. Salo and C. F. Yoder. The dynamics of coorbital satellite systems. *Astronomy and Astrophysics*, 205(1-2):309–327, Oct. 1988.

[16] N. Seto and T. Muto. Relativistic Astrophysics with Resonant Multiple Inspirals. *Physical Review D*, 81(10):103004, May 2010. arXiv: 1005.3114.

[17] J. D. Schnittman. The Lagrange Equilibrium Points L4 and L5 in Black Hole Binary System. *The Astrophysical Journal*, 724(1):39–48, Oct. 2010. Publisher: American Astronomical Society.

[18] J.-L. Lagrange. *Chapitre II: Essai sur le problÄ¨me des trois corps.* Gauthier-Villars, 1867â92.

[19] G. Schafer. Gravitational quadrupole radiation-reaction force and the canonical formalism of ADM. *Ann. Phys. (N.Y.); (United States)*, 161:1, Apr. 1985. Institution: Fakulaet fuer Physik der Universitaet Konstanz, Postfach 5560, D-7750 Konstanz, Federal Republic of Germany.

[20] C. M. Will. On incorporating post-Newtonian effects in N-body dynamics. *Physical Review D*, 89(4):044043, Feb. 2014. arXiv: 1312.1289.

[21] C. M. Will. On the unreasonable effectiveness of the post-Newtonian approximation in gravitational physics. *Proceedings of the National Academy of Sciences*, 108(15):5938–5945, Apr. 2011. arXiv: 1102.5192.

[22] K. Yamada and H. Asada. Nonchaotic evolution of triangular configuration due to gravitational radiation reaction in the three-body problem. *Physical Review D*, 93(8):084027, Apr. 2016. arXiv: 1512.01087.

[23] K. Yamada, T. Tsuchiya, and H. Asada. Post-Newtonian effects on the stability of the triangular solution in the three-body problem for general masses. *Physical Review D*, 91(12):124016, June 2015. arXiv: 1505.04534.

[24] K. Yamada and H. Asada. Triangular solution to general relativistic three-body problem for general masses. *Physical Review D*, 86(12):124029, Dec. 2012. arXiv: 1212.0754.

[25] T. Ichita, K. Yamada, and H. Asada. Post-Newtonian effects on Lagrange's equilateral triangular solution for the three-body problem. *Physical Review D*, 83(8):084026, Apr. 2011. arXiv: 1011.3886.

[26] H. Asada. Gravitational wave forms for a three-body system in Lagrange's orbit: Parameter determinations and a binary source test. *Physical Review D*, 80(6):064021, Sept. 2009. Publisher: American Physical Society.

[27] P. Amaro-Seoane, J. R. Gair, M. Freitag, M. C. Miller, I. Mandel, C. J. Cutler, and S. Babak. Intermediate and Extreme Mass-Ratio Inspirals – Astrophysics, Science Applications and Detection using LISA. *Classical and Quantum Gravity*, 24(17):R113–R169, Sept. 2007. arXiv: astro-ph/0703495.

[28] N. Seto. Relativistic Resonant Relations between Massive Black Hole Binary and Extreme Mass Ratio Inspiral. *Physical Review D*, 85(6):064037, Mar. 2012. arXiv: 1202.4761.

[29] C. M. Will. *Gravity: Newtonian, Post-Newtonian, and General Relativistic*. Jan. 2016. Pages: 9 Publication Title: Gravity: Where Do We Stand? ISBN 978-3-319-20223-5. Springer International Publishing Switzerland ADS Bibcode: 2016gwdw.book....9W.

[30] C. Koenigsdoerffer, G. Faye, and G. Schaefer. The binary black-hole dynamics at the third-and-a-half post-Newtonian order in the ADM-formalism. *Physical Review D*, 68(4):044004, Aug. 2003. arXiv: gr-qc/0305048.

[31] L. E. Kidder. Coalescing binary systems of compact objects to (post${)}^{5/2}$-Newtonian order. V. Spin effects. *Physical Review D*, 52(2):821–847, July 1995. Publisher: American Physical Society.

[32] T. Sauer. *Numerical analysis*. Pearson, Hoboken, NJ?, third edition edition, 2018.

[33] C. D. Murray and S. F. Dermott. *Solar system dynamics*. Jan. 1999. Publication Title: Solar system dynamics by C.D. Murray and S.F. McDermott. (Cambridge ADS Bibcode: 1999ssd..book.....M).

[34] M. Bonetti, E. Barausse, G. Faye, F. Haardt, and A. Sesana. About gravitational-wave generation by a three-body system. *Classical and Quantum Gravity*, 34(21):215004, Nov. 2017. arXiv: 1707.04902.

[35] B. F. Schutz. *A First Course in General Relativity, Second Edition*. Cambridge University Press, 2009.

[36] K. S. Thorne and R. D. Blandford. *Modern Classical Physics*. Sept. 2017.

[37] L. D. Landau and E. M. Lifshitz. *The Classical Theory of Fields*. Pergamon Press, 1971.

[38] S. G. Djorgovski, F. Courbin, G. Meylan, D. Sluse, D. J. Thompson, A. Mahabal, and E. Glikman. Discovery of a Probable Physical Triple Quasar. *The Astrophysical Journal*, 662(1):L1–L5, June 2007. arXiv: astro-ph/0701155.

[39] M. J. Graham, K. E. S. Ford, B. McKernan, N. P. Ross, D. Stern, K. Burdge, M. Coughlin, S. G. Djorgovski, A. J. Drake, D. Duev, M. Kasliwal, A. A. Mahabal, S. van Velzen, J. Belicki, E. C. Bellm, R. Burruss, S. B. Cenko, V. Cunningham, G. Helou, S. R. Kulkarni, F. J. Masci, T. Prince, D. Reiley, H. Rodriguez, B. Rusholme, R. M. Smith, and M. T. Soumagnac. Candidate Electromagnetic Counterpart to the Binary Black Hole Merger Gravitational Wave Event S190521g. *Physical Review Letters*, 124(25):251102, June 2020. arXiv: 2006.14122.

Chapter A
Appendix

A1 Bonetti, et al. Numerical Validation

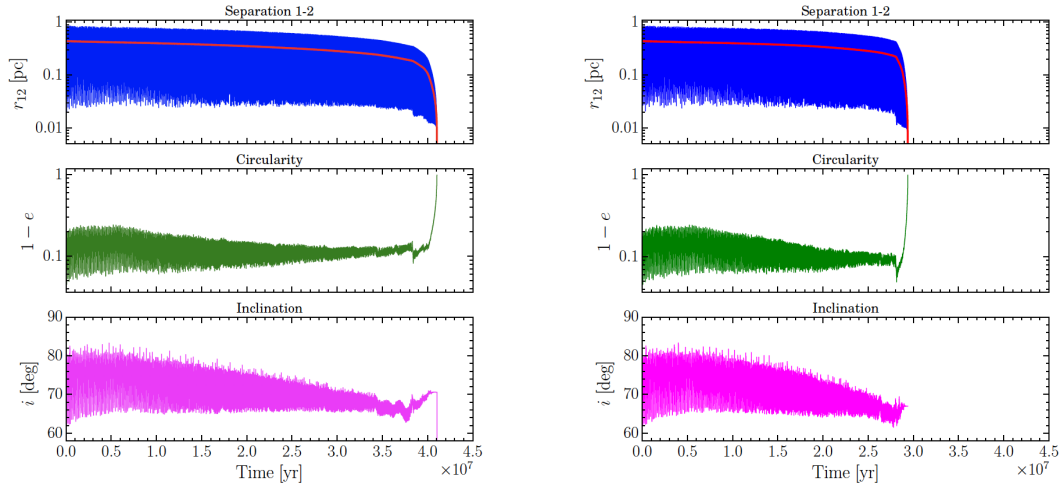

Figure S1: Bonetti, et al. Figure 6, showing the relative separation (upper panels), circularity (middle panels) and inclination (lower panels) for the inner binary of a hierarchical triplet such that $m_1 = 10^9 M_\odot, m2 = 3 \cdot 10^8 M_\odot, m_3 = 5 \cdot 10^8 M_\odot, a_{out} = 4.43pc, e_{out} = 0.5, a_{in} = 0.44pc, e_{in} = 0.8, andi = 80°$*. The solid red line in the separation plot is* a_{in}*. The left figures show quadruple precision calculation and the right figures show double precision calculation [2]. This figure compares to Figure 3.2 displaying qualitatively identical results.*

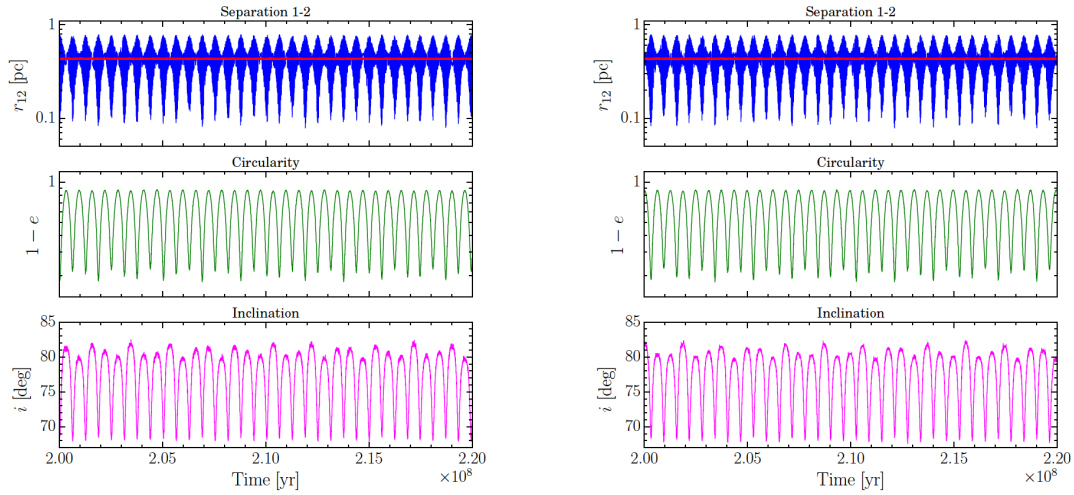

Figure S2: Bonetti, et al. Figure 7, showing the relative separation (upper panels), circularity (middle panels) and inclination (lower panels) for the inner binary of a hierarchical triplet such that $m_1 = 10^9 M_\odot, m2 = 3 \cdot 10^8 M_\odot, m_3 = 5 \cdot 10^8 M_\odot, a_{out} = 4.43pc, e_{out} = 0.5, a_{in} = 0.44pc, e_{in} = 0, andi = 80°$. *The solid red line in the separation plot is* a_{in}. *The left figures show quadruple precision calculation and the right figures show double precision calculation [2]. This figure compares to Figure 3.3 displaying qualitatively identical results.*

A2 Torigoe, et al. Octupole Precision

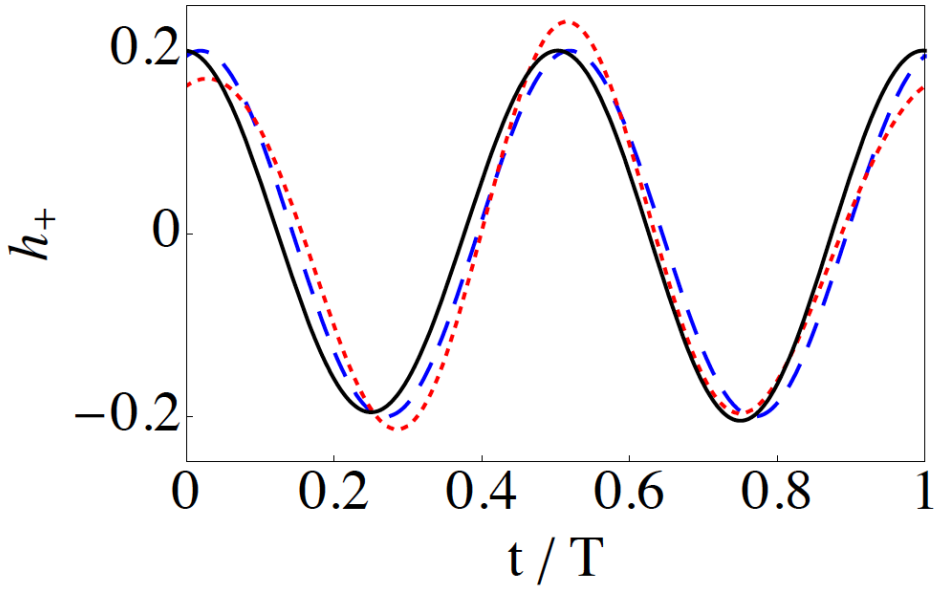

Figure S3: Torigoe et al. Figure 4, showing the gravitational waveforms in arbitrary units for a binary (solid black curve) with $m_1 : m_2 = 2 : 3$ and a Lagrange solution (dotted red and dashed blue curves) with $m_1 : m_2 : m_3 = 1 : 2 : 3$. The quadrupole waveform (dash blue curve) will overlap with the binary (solid black curve) by choosing an initial phase to shift the waveform. Considering the same source, the quadrupole and octupole expansion waveform (dotted red curve) demonstrates variation from the binary (solid black curve) [3].